JOURNAL OF GEOPHYSICAL RESEARCH: ATMOSPHERES, VOL. 118, 3467–3485, doi:10.1029/2012JD018208, 2013

Role of gravity waves in the forcing of quasi two-day waves in the mesosphere: An observational study

M. Ern,[1] P. Preusse,[1] S. Kalisch,[1] M. Kaufmann,[1] and M. Riese[1]

Received 30 May 2012; revised 20 November 2012; accepted 9 December 2012; published 7 May 2013.

[1] Amplitudes of quasi two-day waves (QTDWs) are derived from temperature observations of the High Resolution Dynamics Limb Sounder and Sounding of the Atmosphere using Broadband Emission Radiometry (SABER) satellite instruments. In particular, a global climatology of QTDW amplitudes is derived from 10 years of SABER data, covering the mesosphere and lower thermosphere. This climatology is compared with geostrophic winds and climatologies of gravity wave (GW) momentum flux and GW drag absolute values derived from the same data set. We find that QTDWs are forced shortly after the maximum of the mesospheric summertime zonal wind jet in regions of jet instability where the meridional gradient of quasi-geostrophic zonal mean potential vorticity is strongly negative. The jet instability regions are closely linked to enhanced GW drag that likely seeds those instabilities by decelerating the jet and causing the jet curvature responsible for the negative potential vorticity gradient. The vertical phase structure and the Eliassen-Palm flux of the QTDWs are derived from SABER data and investigated. It is shown that QTDWs propagate upward starting from the jet instability regions. They exert eastward drag in the jet core, and strong westward drag at higher altitudes. Strikingly, the QTDWs are forced in regions where the global distribution of GWs exhibits a characteristic longitudinal structure caused by the GW source patterns in the summer hemisphere. This longitudinal structure might play an important role in the forcing of QTDWs; however, no clear link has been found to the observed QTDW zonal wavenumbers.

Citation: Ern, M., P. Preusse, S. Kalisch, M. Kaufmann, and M. Riese (2013), Role of gravity waves in the forcing of quasi two-day waves in the mesosphere: An observational study, *J. Geophys. Res. Atmos., 118*, 3467–3485, doi:10.1029/2012JD018208.

1. Introduction

[2] The mesosphere is a region very important for atmospheric dynamics. It is governed by a residual circulation pattern, which is directed upward in the summer hemisphere at middle and high latitudes, toward the winter hemisphere at low latitudes, and downward in the winter hemisphere. This residual circulation is driven by atmospheric waves, mainly gravity waves (GWs) [e.g., *Holton*, 1982, 1983]. The upward branch of the mesospheric residual circulation is the reason for the formation of the cold summer mesopause, the coldest region in Earth's atmosphere. These seasonal variations are also the driver of the very strong mesospheric zonal wind jets at middle latitudes, which are westward during summer and eastward during winter. There are also indications of GW-induced coupling effects between summer and winter hemispheres [e.g., *Becker and Fritts*, 2006].

[3] The mesosphere acts as a linking region between the troposphere and stratosphere below, and the thermosphere and ionosphere above. Many dynamical effects (e.g., waves or circulation patterns) that are generated at lower altitudes are also observed in the mesosphere and modulated by mesospheric dynamics before they take effect in the thermosphere and ionosphere where they, for example, can influence the total electron content [e.g., *Borries et al*., 2007; *Chang et al*., 2011; *Hoffmann et al*., 2012] and affect the precision of the GPS. Furthermore, they can modulate atmospheric density and winds in the thermosphere and exosphere [e.g., *Forbes et al*., 2009; *Häusler and Lühr*, 2009; *Oberheide et al*., 2011] with possible implications for the lifetime of satellites.

[4] A prominent example of an atmospheric coupling process is the quasi-biennial oscillation (QBO): The QBO of the zonal wind at low latitudes is a wave-driven circulation pattern in the stratosphere [e.g., *Baldwin et al*., 2001; *Dunkerton*, 1997; *Ern and Preusse*, 2009a, 2009b]. The effects of the QBO are however also observed in different parameters in the mesosphere [e.g., *Baldwin et al*., 2001; *Krebsbach and Preusse*, 2007; *Huang et al*., 2008], and even in thermospheric winds [*Oberheide et al*., 2009]. Another example is tides. Tides are mainly generated in the troposphere by deep convection and latent heat release (nonmigrating tides) or via absorption of solar radiation by ozone and local heating in the stratosphere (migrating tides). Tidal waves propagate upward and can attain large amplitudes in the upper mesosphere and lower thermosphere. A significant effect due to tides is found, for example, in thermospheric

[1]Institut für Energie- und Klimaforschung – Stratosphäre (IEK–7), Forschungszentrum Jülich, 52425, Jülich, Germany.

Corresponding author: M. Ern, Institut für Energie- und Klimaforschung – Stratosphäre (IEK–7), Forschungszentrum Jülich, 52425 Jülich, Germany. (m.ern@fz-juelich.de)

2169-897X/13/2012JD018208

temperatures, densities, and winds [e.g., *Forbes et al*., 2009; *Häusler and Lühr*, 2009; *Oberheide et al*., 2009] or ionospheric electron densities [e.g., *Immel et al*., 2009].

[5] In addition to tidal waves also a number of other global wave modes can be observed in the mesosphere, for example, Rossby waves at middle and high latitudes with typical periods of about 5, 10, and 16 days, fast Kelvin waves and Rossby-gravity waves at low latitudes (both equatorial wave modes), as well as quasi two-day waves (QTDWs). Climatologies of different wave modes have been derived in a number of different studies [e.g., *Garcia et al*., 2005; *Pancheva et al*., 2009a, 2009b, 2010; *Ern et al*., 2009; *Mukhtarov et al*., 2009; *Tunbridge et al*., 2011]. Because our current study is focused on the QTDW and its forcing, an introduction to the main findings about QTDWs is given in the following.

[6] The occurrence of QTDWs in mesospheric wind data observed by radars has now been reported for over 40 years [e.g., *Müller*, 1972]. QTDWs are one of the largest amplitude planetary wave modes in the mesosphere. Temperature amplitudes can reach up to about 11 K in the altitude range 80–100 km [e.g., *Limpasuvan and Wu*, 2003]. In the upper mesosphere, wind amplitudes can be up to about 50 m/s in the meridional wind at low latitudes [e.g., *Fritts et al*., 1999], and up to about 30 m/s in the zonal wind at middle latitudes [e.g., *Thayaparan et al*., 1997]. Signatures of the QTDW are also found in atmospheric constituent data [e.g., *Azeem et al*., 2001]. QTDWs travel westward and have wave periods in the range of about 40–60 h [e.g., *Hecht et al*., 2010; *Tunbridge et al*., 2011]. Sometimes phase-locking with tidal modes is observed [e.g., *Hecht et al*., 2010]. Zonal wavenumbers observed are mainly $k=3$ or $k=4$, and somewhat weaker also $k=2$. This has been shown, for example, in a climatology of QTDWs based on temperature observations of the Microwave Limb Sounder onboard the EOS-Aura satellite (MLS/Aura) [*Tunbridge et al*., 2011]. QTDWs occur in the summer hemisphere shortly after the summer solstices in short bursts of wave activity, about 20–60 days long [e.g., *Wu et al*., 1996; *Limpasuvan and Wu*, 2003; *Ern et al*., 2009; *Tunbridge et al*., 2011]. Peak wave activity is observed about one month after the solstices. Especially in the upper mesosphere and lower thermosphere, QTDWs are also able to penetrate from the summer into the winter hemisphere [e.g., *Ern et al*., 2009; *Tunbridge et al*., 2011].

[7] Ground-based phase speeds of QTDWs at 30° latitude are about 100, 70, and 50 m/s westward for zonal wavenumbers 2, 3, and 4, respectively. These phase speeds often exceed the wind speed of the summertime mesospheric westward wind jet. Therefore, QTDWs usually do not encounter critical wind levels on top of this wind jet, and they can propagate toward higher altitudes. Effects due to QTDWs are not only observed in the mesosphere and lower thermosphere, but also in the ionosphere up to altitudes of several hundred kilometers [e.g., *Altadill et al*., 1998; *Forbes and Zhang*, 1999; *Gurubaran et al*., 2001; *Pancheva et al*., 2006; *Liu et al*., 2010; *Pedatella and Forbes*, 2012]. Possible mechanisms to explain QTDW signals at these high altitudes could be, for example, indirect effects such as interactions between the QTDW and tides or GWs [e.g., *Meyer*, 1999; *Liu et al*., 2010].

[8] There is still large uncertainty about how QTDWs are excited. QTWDs with zonal wavenumbers $k=3$ and 4 show the characteristic behavior of atmospheric normal modes [e.g., *Salby*, 1984; *Tunbridge et al*., 2011]. However, the observed global structure of QTDWs cannot be fully explained by a simple approach assuming forcing of the normal modes in the troposphere [e.g., *Jacobi et al*., 2006], and it has been more and more accepted that jet instabilities of the summertime mesospheric easterly zonal wind jet play an important role by either directly exciting QTDWs [e.g., *Plumb*, 1983; *Pfister*, 1985; *Randel*, 1994], or by amplifying the normal modes due to local instabilities [e.g., *Salby and Callaghan*, 2001; *Rojas and Norton*, 2007].

[9] The meridional gradient of the quasi-geostrophic zonal mean potential vorticity (PV) is given by

$$\frac{\partial \bar{Q}}{\partial y} = \beta - \frac{1}{a^2}\frac{\partial}{\partial \varphi}\left[\frac{1}{cos\varphi}\frac{\partial}{\partial \varphi}(\bar{u}cos\varphi)\right] - \frac{1}{\rho_0}\frac{\partial}{\partial z}\left[\rho_0 \frac{f^2}{N^2}\frac{\partial \bar{u}}{\partial z}\right] \quad (1)$$

with y the meridional coordinate, z the vertical coordinate, φ the geographic latitude, a the Earth radius, f the Coriolis parameter, β the meridional gradient of f, N the buoyancy frequency, ρ_0 the background density, and $\bar{u}$ the zonal mean zonal background wind [see also *Salby and Callaghan*, 2001]. The summertime mean westward background flow is destabilized if $\partial \bar{Q}/\partial y$ becomes negative. This is the case if there are strong meridional and/or vertical curvatures of the zonal wind jet that overcompensate the stabilizing effect of β. Negative values of $\partial \bar{Q}/\partial y$ can be taken as indicator for regions or time periods that are favorable for the forcing of QTDWs [e.g., *Plumb*, 1983; *Pfister*, 1985; *Norton and Thuburn*, 1996; *Salby and Callaghan*, 2001; *Offermann et al*., 2011].

[10] Some studies indicate that inertial instabilities at the equatorial stratopause can trigger jet instabilities close to the equator that can lead to the excitation of QTDWs [e.g., *Orsolini et al*., 1997; *Limpasuvan et al*., 2000]. These studies give realistic results in some aspects; however, GWs probably play a more important role in the forcing of QTDWs. Several studies indicate that strong instabilities of the zonal wind jets are seeded by GWs [e.g., *Norton and Thuburn*, 1996; *Pendlebury*, 2012]. In particular, the occurrence of QTDWs in models is very sensitive to the settings of the GW drag scheme [e.g., *Norton and Thuburn*, 1996]. Also, observations indicate the importance of GWs for the forcing of QTDWs [e.g., *Limpasuvan and Wu*, 2003].

[11] Still, the role of GWs is not fully understood. It has been shown by *Holton* [1984] that longitudinal structures in the zonal wind forcing by GWs (GW drag) are a possible source of planetary-scale waves in the mesosphere, and it has been speculated that observed zonal nonuniformities in the global distribution of GWs could also play an important role in the forcing of QTDWs [e.g., *Limpasuvan and Wu*, 2003; *Ern et al*., 2011]. These nonuniformities are likely introduced by the longitudinal distribution of deep convection in the subtropics of the summer hemisphere and become important at middle latitudes in the mesosphere because of the poleward refraction of GWs into the strong mesospheric wind jets [see also *Sato et al*., 2009; *Preusse et al*., 2009b; *Ern et al*., 2011]. To some extent GW sources at middle latitudes will also contribute to the observed characteristic longitudinal distribution of GWs [e.g., *Hoffmann and Alexander*, 2010].

[12] Furthermore, the temporal evolution of the global distribution of GWs, their forcing of the mesospheric zonal wind jets, and possible relations to the occurrence of QTDWs

have still not been studied. Recently, global observations of GW momentum flux and GW drag absolute values in the mesosphere became available [*Ern et al*., 2011]. With these new data sets it is now possible to study the global distribution of GWs, their interaction with the background wind, and, hence to study the role of GWs in the forcing of QTDWs based on observational data.

[13] In section 2 the satellite instruments High Resolution Dynamics Limb Sounder (HIRDLS) and Sounding of the Atmosphere using Broadband Emission Radiometry (SABER) are briefly introduced, and we explain how the data sets used for our current analysis are generated (global distributions of QTDW amplitudes, quasi-geostrophic winds, the PV gradient $\partial\bar{Q}/\partial y$, GW momentum flux, and GW drag). QTDW distributions are analyzed together with the other data sets in section 3. This is conducted step by step. We first focus on the temporal evolution and then provide time-averaged zonal mean distributions for all parameters, as well as time-averaged longitudinal distributions of GWs. A number of implications for the forcing of QTDWs are derived from these comparisons. Furthermore, the Eliassen-Palm flux (EP flux) and flux divergence of the QTDWs are determined and discussed. Finally, the results are summarized in section 4.

2. Instruments and Data Sets

2.1. The Satellite Instruments HIRDLS and SABER

[14] Our study is mainly based on temperatures observed by the satellite instruments HIRDLS (onboard the EOS-Aura satellite) and SABER (onboard the TIMED satellite). HIRDLS and SABER are both infrared limb sounders. Atmospheric temperatures are derived from the 15 μm emission of CO_2. For our study we use HIRDLS version V006 and SABER version v1.07 data. HIRDLS observations cover the time period from January 2005 until March 2008. SABER observations start in January 2002 and are still ongoing at the time of writing. Observations of both instruments are near-global. The latitudinal coverage is about 63°S to 80°N for HIRDLS. The latitudinal coverage for SABER is about 50°S to 82°N or 82°S to 50°N, switching every ~60 days due to yaw maneuvers of the TIMED satellite. Altitude coverage is from the tropopause region to about 75 km for HIRDLS, and from the tropopause region to well above 100 km for SABER.

[15] Further information about the HIRDLS instrument and temperature retrieval can be found, for example in *Gille et al*. [2003, 2008]. More information about the SABER instrument and temperature retrieval are available, for example, in *Mlynczak* [1997], *Russell et al*. [1999], or *Remsberg et al*. [2004, 2008].

2.2. Global Distribution of Quasi Two-Day Wave Temperature Amplitudes

2.2.1. Method

[16] Longitude-time spectra have been determined from HIRDLS and SABER temperature observations for a set of fixed latitudes and altitudes in overlapping time windows of 31 days length. By combining ascending and descending orbit parts (i.e., satellite overpasses of a latitude circle with increasing or decreasing latitude, respectively), waves with frequencies lower than about 1 cycle/d and zonal wavenumbers up to 6 can be resolved by the satellite sampling pattern. These ranges apply for both eastward and westward travelling waves. More technical details can be found, for example, in *Ern et al*. [2008, 2011].

[17] To extract the signal of QTDWs a band-pass has been applied and only spectral contributions of westward propagating waves with frequencies between 0.3 and 0.7 cycles/d (corresponding to wave periods between about 1.4 and 3.3 days) are used. This spectral band is mainly dominated by QTDWs, and particularly during summertime in the mesosphere these spectral contributions can be attributed almost solely to QTDWs. For only these spectral contributions a backward transformation is carried out and daily global maps of residual temperatures are calculated at 00:00 GMT for all days of the HIRDLS mission from January 2005 until March 2008, as well as for 10 years of SABER data from 2002 to 2011. These global distributions are calculated on a three-dimensional grid with a resolution of 10° longitude × 1° latitude × 0.5 km altitude. To reduce the effect of GWs, smoothing by 5 km vertically was applied. The true latitudinal resolution is determined by the along-track sampling of the satellite instruments, and is (at middle and low latitudes) about 1° for HIRDLS and about 4° for SABER. Daily estimates of QTDW amplitudes for different zonal wavenumbers are obtained by carrying out a Fourier analysis of the daily global maps in the longitudinal direction for every 1° latitude.

[18] It has been shown that the temporal evolution of global wave modes can be captured even if a spectral band-pass is applied to longitude-time spectra [e.g., *Ern et al*., 2008]. Nevertheless, in the following subsection the reliability of our approach is checked by comparison with results of *Tunbridge et al*. [2011] using a complementary analysis method particularly dedicated to QTDWs.

[19] Aliasing effects caused by the asynoptic nature of the satellite sampling pattern have been investigated in detail by *Tunbridge et al*. [2011]. Because our method and the one employed by *Tunbridge et al*. [2011] are similar, the main findings of this investigation are also valid for our study. In particular, *Tunbridge et al*. [2011] find that eastward travelling global-scale waves with two-day period and zonal wavenumbers 1, 2, and 3 can be aliased on the westward travelling QTDWs with zonal wavenumbers 2, 3, and 4, respectively. These eastward travelling waves are known to exist at high latitudes in the winter hemisphere, and aliasing will affect amplitudes and phases of QTDWs determined in this region. However, in the summer hemisphere the activity of these eastward travelling waves is usually very low, and aliasing will probably not pose a major problem for the analysis of QTDWs [*Tunbridge et al*., 2011]. Because our study is focused on the QTDW activity in the summer hemisphere, also our results are probably not affected much by aliasing.

2.2.2. Comparison With the Quasi Two-Day Wave Analysis by *Tunbridge et al*. [2011]

[20] For validation purposes, we compare our results to temperature amplitudes shown in Figure 10 of *Tunbridge et al*. [2011], who analyzed over 5 years of temperature observations by the MLS/Aura satellite instrument. The values shown in their Figure 10 represent averages over the period April 2004 until September 2009 and are at 40° latitude and 81 km altitude. Values are given for both Northern and Southern Hemispheres.

[21] We have calculated the same averages for the SABER QTDW data set described above. Some care has to be taken

because the analysis by *Tunbridge et al*. [2011] is based on 12 day time-windows. Furthermore, at this altitude the vertical resolution of MLS/Aura is only about 13 km [e.g., *Schwartz et al*., 2008]. Therefore, our SABER analysis has been smoothed vertically by 13 km and also by 13 days in time to fully match the characteristics of the analysis by *Tunbridge et al*. [2011].

[22] The comparison is shown in Figure 1. In this figure, values obtained from our analysis are given as blue lines, whereas the other colored lines reproduce the results by *Tunbridge et al*. [2011]. Results are shown for zonal wavenumbers $k=2$ (Figure 1a), $k=3$ (Figure 1b), and $k=4$ (Figure 1c). Dashed lines are for the Southern Hemisphere in January/February and solid lines for the Northern Hemisphere in July/August.

[23] Obviously, there is a very good overall agreement between SABER and MLS/Aura QTDW amplitudes for all zonal wavenumbers shown and in both Northern and Southern Hemispheres. Only QTDW activity for zonal wavenumber 4 in the Northern Hemisphere seems to extend somewhat longer in the MLS/Aura observations. Possible reasons might be differences in details of the analysis techniques, or possible effects of data gaps in one or both data sets. Apart from those minor differences it is clearly shown that both amplitude and temporal evolution of QTDW bursts are well captured by our analysis.

2.2.3. Comparison of SABER and HIRDLS Quasi Two-Day Wave Amplitudes

[24] For another cross-check we compare HIRDLS and SABER QTDW amplitudes at 65 km altitude and 30°S, as well as 30°N, during summer of the respective hemisphere, averaged over the whole time period that is covered by both instruments (i.e., January 2005 until March 2008). This altitude and these latitudes have been chosen because it turns out that this is an important region, directly located above core regions of QTDW forcing (see also section 3).

[25] The results are shown in Figure 2. The upper (lower) row in Figure 2 shows QTDW amplitudes in the Southern (Northern) Hemisphere at 30°S (30°N). The left column shows amplitudes for QTDWs with zonal wavenumber $k=3$, the right column for $k=4$. Red lines stand for QTDW amplitudes derived from HIRDLS temperatures, blue lines show the same, but for SABER. The time on the x-axis is given in days of the year ("doy"). For the Southern Hemisphere (upper row) the time range shown is from 27 November until 5 March, for the Northern Hemisphere (lower row) from 27 May until 5 September. We find good agreement between HIRDLS and SABER QTDW amplitudes at both latitudes, and for both zonal wavenumbers 3 and 4. Minor differences may arise from differences in the temporal coverage of both instruments.

2.3. Global Distributions of Gravity Wave Momentum Flux and Gravity Wave Drag

2.3.1. Gravity Wave Momentum Flux

[26] Absolute values of GW momentum flux have been derived from subsequent pairs of temperature altitude profiles along the satellite measurement track for the satellite instruments HIRDLS and SABER [*Ern et al*., 2011]. The large-scale atmospheric background was estimated by two-dimensional spectral decomposition of the temperature fields in longitude and time, (see also section 2.2.1). This background covering global-scale waves up to zonal wave-number 6 is subtracted from the single altitude profiles to obtain residual temperatures that can be attributed to GWs. With this method it is also possible to estimate short-period global-scale waves with periods as short as about 1–2 days. This is especially important for our current study because temperature fluctuations due to GWs can be cleanly separated from QTDWs. For more details see *Ern et al*. [2011]. In addition to the method described in *Ern et al*. [2011], tides up to zonal wavenumber 4 have been removed. Because ascending and descending orbit segments are at different but nearly-fixed local times, tidal modes appear as stationary wave patterns if only ascending or only descending orbit parts are considered [e.g., *Preusse et al*., 2001] and can be subtracted.

[27] Gravity wave amplitudes and vertical wavelengths for the strongest waves found in each altitude profile are determined from moving 10 km vertical windows [see *Preusse et al*., 2002; *Ern et al*., 2004]. Horizontal wavelengths are determined from vertical phase shifts of GWs found in subsequent pairs of altitude profiles along the measurement track [*Ern et al*., 2004, 2011]. Absolute values of the vertical

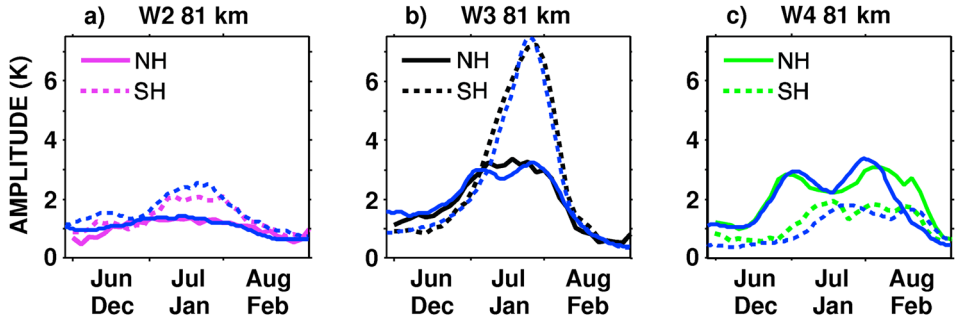

Figure 1. Quasi two-day wave amplitudes at 81 km altitude during December until February at 40°S (dashed) and during June until August at 40°N (solid). Shown are amplitudes for zonal wavenumbers (a) $k=2$, (b) $k=3$, and (c) $k=4$. All values are averages over the period April 2004 until September 2009. Blue lines represent this study based on SABER temperatures, other colors represent values obtained in the study by *Tunbridge et al*. [2011] based on MLS/Aura temperature data. This figure has been reproduced and modified from Figure 10 in *Tunbridge et al*. [2011]. Copyright [2011] American Geophysical Union. Reproduced/modified by permission of American Geophysical Union.

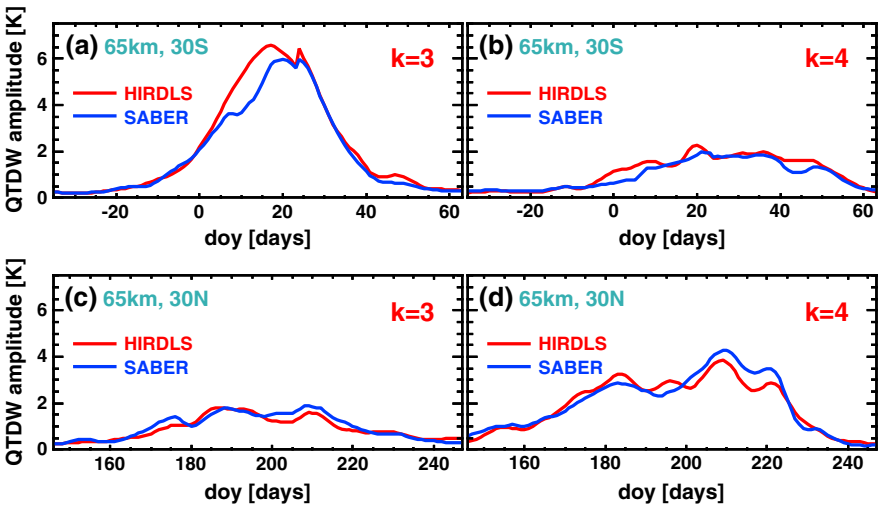

Figure 2. Average quasi two-day wave amplitudes at 65 km altitude. Shown are amplitudes for zonal wavenumbers (a) $k=3$ and (b) $k=4$ at 30°S, and (c) $k=3$ and (d) $k=4$ at 30°N. Values represent averages over the period January 2005 until March 2008. QTDW amplitudes were derived from (blue) SABER and (red) HIRDLS temperatures. Time on the x-axes is given in doy (day of the year). The periods shown are 27 November until 5 March (upper row) and 27 May until 5 September (lower row).

flux of horizontal momentum due to GWs are calculated via equation (7) in *Ern et al.* [2004]:

$$F_{\mathrm{ph}} = \frac{1}{2}\,\varrho_0\,\frac{\lambda_z}{\lambda_h}\left(\frac{g}{N}\right)^2\left(\frac{\hat{T}}{T}\right)^2 \tag{2}$$

with ϱ_0 the atmospheric background density, g the gravity acceleration, N the buoyancy frequency, λ_h and λ_z the horizontal and vertical wavelength of the GW, $\hat{T}$ the temperature amplitude of the GW, and T the atmospheric background temperature. All GW momentum fluxes and also GW drag (see the following subsection) used in this study are derived from SABER observations. Estimates presented are representative for GWs with vertical wavelengths in the range 4–25 km and horizontal wavelengths longer than about 100–200 km (see also, for example, *Preusse et al.* [2002, 2009a], *Alexander et al.* [2010], or *Ern et al.* [2011]).

[28] Because pairs of altitude profiles provide only two-dimensional information, no information about the propagation direction of GWs can be obtained and only absolute values of momentum flux can be determined. Uncertainties of these absolute values are large, at least a factor of 2 [e.g., *Ern et al.*, 2004, 2011]. SABER GW momentum fluxes presented in this study will also be somewhat low-biased with respect to the estimates derived by *Ern et al.* [2004] that contain additional corrections and that were validated by superpressure balloons [*Hertzog et al.*, 2008].

2.3.2. Gravity Wave Drag

[29] From vertical gradients of these GW momentum fluxes, absolute values of wind tendencies due to GWs (GW drag) can be estimated

$$XY = -\frac{1}{\varrho_0}\frac{\partial F_{\mathrm{ph}}}{\partial z} \tag{3}$$

[30] with XY the acceleration or deceleration of the background wind, ϱ_0 the atmospheric background density, F_{ph} the absolute value of GW momentum flux, and z the vertical coordinate. Because no directional information is available for F_{ph}, also XY does not contain any directional information, i.e., we can only estimate GW drag absolute values. Therefore, values of XY are always positive. Like for GW momentum flux absolute values, uncertainties are large. Furthermore, like the momentum fluxes, values of XY are representative only of part of the whole GW spectrum, and therefore they do not represent the whole GW drag term of the overall momentum budget. For more details see also *Ern et al.* [2011].

[31] Under certain conditions the prevalent GW propagation direction is known from theoretical considerations, as well as model simulations. It has been shown by *Warner et al.* [2005] that in strong wind jets the GW spectrum is filtered such that the GW spectrum in the upper part of the jet and directly above is dominated by GW momentum opposite to the jet direction. The theoretical part of the study has been checked by comparison with the GW propagation directions observed by radiosondes, and good agreement is found. This filtering effect is seen for both the QBO and the semiannual oscillation in the tropics, and, of course, in the much stronger mesospheric wind jets the wind filtering of the GW spectrum is even more effective. A good illustration of this filtering effect can be found, for example, in *Beres* [2005]. This paper addresses the effect of wind filtering on the GW spectra associated with a longitudinally nonuniform distribution of convective GW sources, i.e., exactly the situation relevant for our study. The results by *Beres* [2005] confirm the results by *Warner et al.* [2005] and demonstrate that in the summertime mesospheric wind jet and at its top GW momentum flux is strongly dominated by the direction opposite to the jet. Consequently, observed GW momentum flux absolute values (i.e., the total observed GW momentum flux) can almost completely be attributed to this direction.

[32] Because a large part of the total momentum flux is covered by this direction, also strong negative vertical gradients in the total observed momentum flux can in most cases

be attributed to this propagation direction, and the resulting (total) GW drag will be mainly opposite to the wind jet. This is even more the case for wind reversals at the top of a strong wind jet (an important case in our study). The critical amplitude threshold for the onset of wave breaking is proportional to the difference between background wind speed and the phase speed of a GW (see for example, *Ern et al*. [2008], equation (10)). Therefore, GWs propagating opposite to the wind jet can attain larger amplitudes and carry stronger momentum than GWs propagating into other directions. During a wind reversal at the top of a wind jet part of the waves propagating opposite to the jet will encounter critical wind levels and dissipate. However, even the waves propagating opposite to the jet that do not encounter critical wind levels are strongly affected, because the critical wave amplitude threshold for the onset of GW breaking is strongly reduced as the difference between wave phase speed and wind speed is reduced during the wind reversal. Accordingly, the waves will lose momentum, and the resulting wave drag will be opposite to the wind direction in the jet.

[33] Even though there are large uncertainties inherent in the method, SABER GW momentum fluxes and GW drag are currently the only observational global data sets of this kind available in the mesosphere, and they provide valuable information and a global picture of the interaction of GWs with the background winds.

[34] The global estimates of GW momentum fluxes and GW drag that are used in this study are 7 day averages with a time step of 3 days. A temporal resolution better than the monthly averages previously used by *Ern et al*. [2011] is required for comparison with the very short bursts of QTDW activity (sometimes as short as only 20 days). Momentum flux and GW drag are determined on a longitude/latitude/altitude grid of $10^\circ \times 2^\circ \times 0.5$ km. Compromising between a statistically meaningful number of profiles in the single bins and sufficient spatial resolution, the data are mapped into overlapping bins of 30° longitude × 20° latitude, centered at the grid points. The vertical resolution of 10 km is governed by the vertical windows used, see above.

2.4. Estimation of Quasi-Geostrophic Winds

[35] Wind observations in the mesosphere are sparse, mostly limited to single observing stations, and also limited in their vertical coverage. Therefore, for our study we calculate quasi-geostrophic winds from SABER temperature, geopotential and pressure data. This calculation is mainly based on the approach by *Oberheide et al*. [2002]. Following *Andrews et al*. [1987], the momentum budget in hydrostatic equilibrium can be written as follows:

$$\frac{Du}{dt} - \left(f + \frac{\mathrm{u}\tan\varphi}{a}\right)v + \frac{1}{a\cos\varphi}\frac{\partial\Phi}{\partial\lambda} = X \tag{4}$$

$$\frac{Dv}{dt} + \left(f + \frac{u\tan\varphi}{a}\right)u + \frac{1}{a}\frac{\partial\Phi}{\partial\varphi} = Y \tag{5}$$

with λ and φ the geographic longitude and latitude, u and v the zonal and the meridional wind, D/Dt is the total differential in time, f the Coriolis parameter, Φ the geopotential, and X and Y are friction terms in zonal and meridional direction, respectively.

[36] For stationary conditions and zero friction these equations can be rewritten as follows:

$$-\left(f + \frac{u\tan\varphi}{a}\right)v + \frac{1}{a\cos\varphi}\frac{\partial\Phi}{\partial\lambda} = 0 \tag{6}$$

$$\left(f + \frac{u\tan\varphi}{a}\right)u + \frac{1}{a}\frac{\partial\Phi}{\partial\varphi} = 0 \tag{7}$$

[37] These two equations can be easily solved for u and v. At low latitudes (equatorward of 11°), values are obtained by linear interpolation, starting from subtropical values. This is required as f becomes zero at the equator, and close to the equator winds derived from equations (6) and (7) are therefore not reliable. See also *Oberheide et al*. [2002].

[38] Quasi-geostrophic winds have been shown to be in good agreement with radar observations [e.g., *Oberheide et al*., 2002]. However, the friction terms X and Y are neglected in equations (6) and (7). These friction terms include, for example, drag exerted by atmospheric waves. Especially in the upper mesosphere, GW drag becomes increasingly important for the momentum budget of the zonal wind jets. Therefore, quasi-geostrophic winds in the mesosphere will likely be somewhat high-biased.

[39] Quasi-geostrophic winds are determined on a three-dimensional grid of $10^\circ \times 2^\circ \times 0.5$ km resolution in longitude, latitude, and altitude, respectively. The true resolution given by our binning of the data and the vertical field-of-view of SABER is about $50^\circ \times 10^\circ \times 2$ km in longitude, latitude, and altitude. In the meridional direction a variable resolution is used, depending on the SABER global data coverage. The true meridional resolution is about 10° at mid and low latitudes, and better at high latitudes. This good meridional resolution is important, because quasi-geostrophic winds will be compared with high resolution distributions of QTDW amplitudes (see above). Furthermore, for an estimation of $\partial\bar{Q}/\partial y$ both good meridional and vertical resolution are required.

[40] To match the temporal resolution of our GW data sets, quasi-geostrophic winds are determined for the same time intervals as the GW data (7 day averages with a time step of 3 days). Because above 80 km altitude tides become increasingly important and might bias zonal averages, only quasi-geostrophic winds below this altitude are used for our study.

2.5. Time Series of the Data Sets Used

[41] Figure 3 shows an overview of the data sets used in this study. Shown are latitude-time cross-sections for the years 2002–2011. Winds, the PV gradient $\partial\bar{Q}/\partial y$ and QTDW amplitudes are shown at 65 km altitude, i.e., somewhat above the core region of QTDW forcing (see section 3) to allow for some amplitude growth of the QTDWs. GW momentum flux and GW drag are shown at 60 km altitude.

[42] Quasi-geostrophic winds at 65 km altitude (Figure 3a) alternate between summertime easterlies and wintertime westerlies in the mesosphere. Our peak values are somewhat higher than peak values found in the Stratospheric Processes And their Role in Climate (SPARC) zonal wind climatology [see also *Swinbank and Ortland*, 2003; *Randel et al*., 2002, 2004], but comparable to the Committee On Space Research (COSPAR) International Reference Atmosphere (CIRA-86) wind climatology, which in the stratosphere and mesosphere

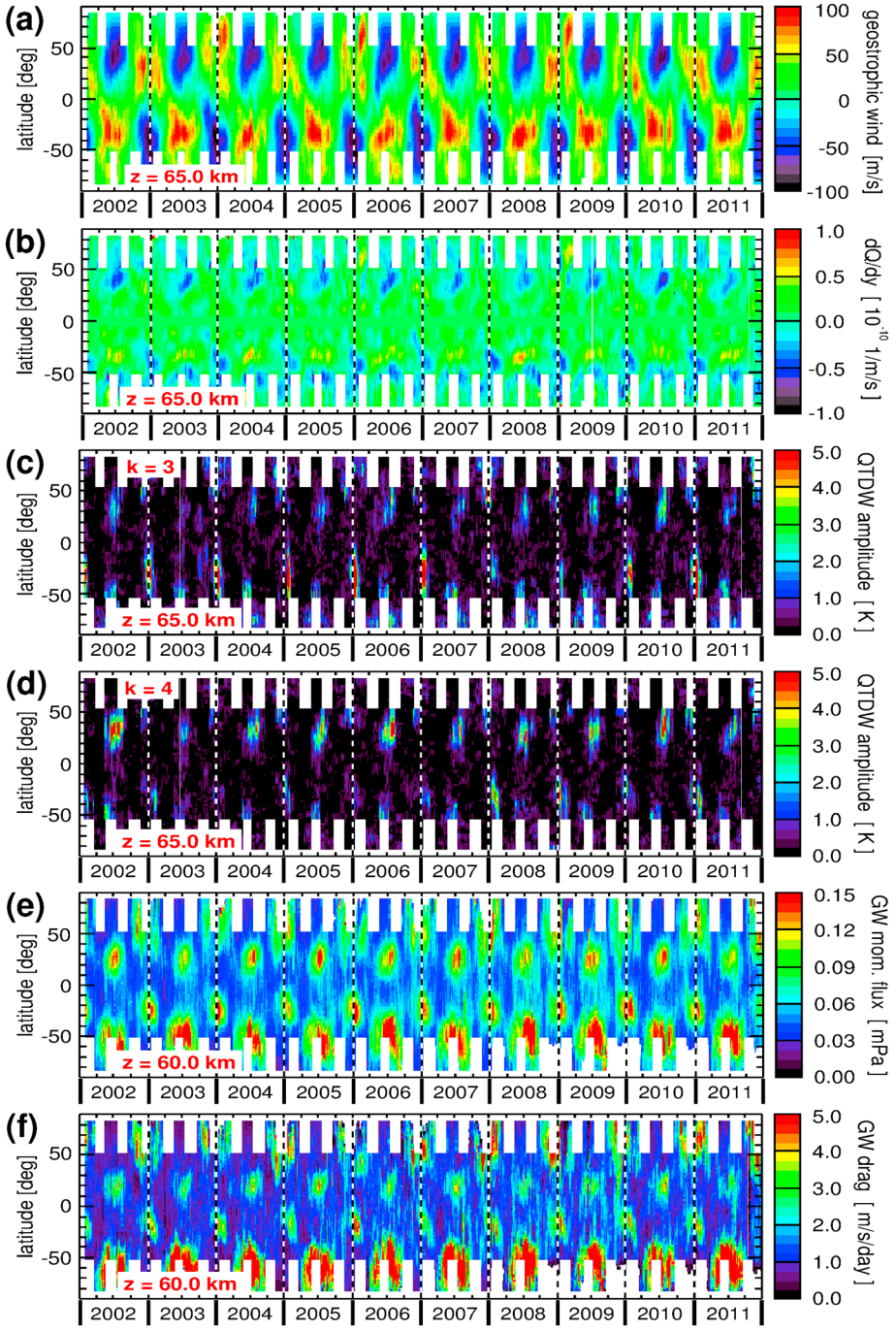

Figure 3. Latitude-time cross-sections for the years 2002–2011 at 65 km altitude of SABER (a) quasi-geostrophic zonal winds, (b) meridional gradients of the quasi-geostrophic potential vorticity, (c) quasi two-day wave amplitudes for zonal wavenumber $k=3$, and (d) $k=4$. Furthermore, latitude-time cross-sections at 60 km altitude are shown for SABER (e) gravity wave momentum flux and (f) gravity wave drag absolute values.

also represents geostrophic winds determined from satellite data [see also *Fleming et al.*, 1990].

[43] Meridional gradients of the quasi-geostrophic zonal mean PV ($\partial\bar{Q}/\partial y$, cf. equation (1)) calculated from these winds are shown in Figure 3b. Negative values that are indicative of jet instabilities can be found especially in the summer hemisphere poleward of about 30° latitude. They follow the shape of the westward summertime mesospheric wind jets and shift poleward with time.

[44] In Figures 3c and 3d wave amplitudes for zonal wavenumbers $k=3$ and $k=4$, respectively, are shown for 65 km altitude. Enhanced wave amplitudes that occur in the summer hemispheres at middle latitudes can be attributed to QTDWs. As has been found before [e.g., *Tunbridge et al.*,

2011], in the Northern Hemisphere QTDWs with zonal wavenumber $k=4$ are usually somewhat stronger than QTDWs with $k=3$. Different from this, in the Southern Hemisphere usually QTDWs with $k=3$ are considerably stronger than those with $k=4$. Only in the years 2008 and 2009 QTDWs with $k=4$ are stronger also in the Southern Hemisphere [see also *Tunbridge et al.*, 2011]. Strongest QTDW activity is observed between about 20° and 40° latitude. Maxima in wintertime at high latitudes are due to fast eastward travelling waves of wavenumber 2 (3), which are aliased with reduced amplitude on westward wavenumbers 3 (4) [*Tunbridge et al.*, 2011] and are therefore not the QTDWs discussed in this paper.

[45] Figure 3e shows SABER GW momentum flux absolute values at 60 km altitude. Enhanced values are found both in the wintertime westerly and in the summertime easterly mesospheric jets. In these jets momentum fluxes are enhanced because GWs that propagate opposite to the prevailing wind direction can attain large amplitudes before wave breaking takes place [e.g., *Preusse et al.*, 2006, 2008]. Consequently, these waves dominate the observed GW distribution in strong wind jets and also directly on top of the jet [*Warner et al.*, 2005; *Ern et al.*, 2006]. Enhanced wave activity in the summertime mesospheric jets is likely caused by GWs generated by convection, shear instability, or other source processes in the summer hemisphere

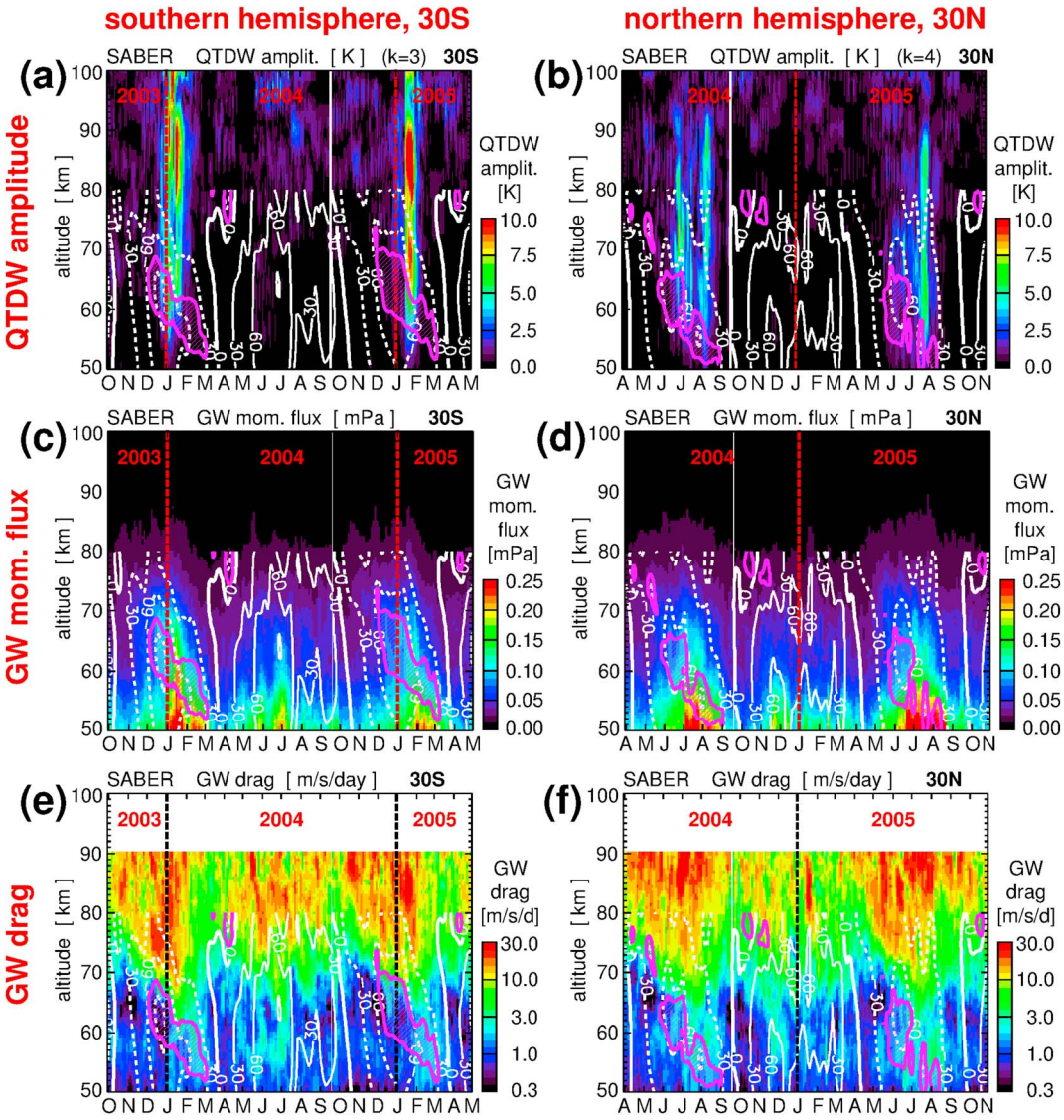

Figure 4. Altitude-time cross-sections for the periods October 2003 until April 2005 at 30°S in the Southern Hemisphere (left column) and for the period April 2004 until October 2005 at 30°N in the Northern Hemisphere (right column). In the upper row SABER QTDW amplitudes are given for zonal wavenumber (a) $k=3$ in the Southern Hemisphere and (b) $k=4$ in the Northern Hemisphere. The middle row shows SABER GW momentum flux absolute values in mPa (i.e., 10^{-3} Pa), and the bottom row SABER GW drag absolute values in m/s/d. In all panels white contour lines represent SABER zonal mean quasi-geostrophic zonal winds in m/s. Contour increment is 30 m/s, dashed lines indicate westward wind. Magenta hatched areas indicate regions of strongly negative meridional gradients of the quasi-geostrophic zonal mean PV ($\partial\bar{Q}/\partial y < -2 \times 10^{-11}$ 1/m/s).

subtropics. These waves shift poleward during their upward propagation [*Sato et al*., 2009; *Preusse et al*., 2009b; *Ern et al*., 2011]. However, GW sources during summertime at middle latitudes might also contribute [e.g., *Hoffmann and Alexander*, 2010].

[46] Figure 3f shows GW drag absolute values at 60 km altitude derived from vertical gradients in GW momentum flux absolute values. Values are smoothed vertically by a running mean of 5 km width [see also *Ern et al*., 2011]. Like the momentum fluxes, values are enhanced in the mesospheric jets during both summertime and wintertime. Please note that the maxima of GW momentum flux in the summertime jet are located on the equatorward side of the jet, and GW drag maxima are located even somewhat more equatorward.

3. Relationship Between Zonal Winds, Quasi Two-Day Waves, and Gravity Waves

3.1. Identification of Quasi Two-Day Wave Forcing Regions in Altitude-Time Cross-Sections

[47] We will now study the temporal evolution of zonal winds on one hand, and QTDW and GW activity on the other. As has been seen from Figure 3, QTDW activity is highest between about 20° and 40° latitude. Therefore, we will investigate altitude-time cross-sections that are located at 30° latitude, i.e., in the center of this range. We have selected two time periods, one for the Northern, and another for the Southern Hemisphere, each covering two QTDW bursts. By selecting certain time periods with full temporal resolution we preserve the fine structures that would average out in, for example, averages calculated over the whole SABER mission.

3.1.1. Observed Variations of Zonal Wind, QTDWs and GWs

[48] Figure 4 shows altitude-time cross-sections of QTDW amplitudes (upper row), GW momentum flux (middle row), and GW drag (lower row). The left column is at 30°S for the period October 2003 until May 2005, and the right column is at 30°N for the period April 2004 until November 2005. Both time periods shown cover two periods of QTDW activity in the respective summer hemisphere. For the Southern (Northern) Hemisphere amplitudes for the QTDW with zonal wavenumber 3 (4) are shown. In all panels SABER zonal mean quasi-geostrophic zonal winds are given as white contour lines. Westward winds are dashed and eastward winds are indicated by solid lines. The magenta hatched areas also given in all panels highlight regions of zonal wind jet instabilities where the meridional gradient of the quasi-geostrophic PV $\partial\bar{Q}/\partial y$ is more strongly negative than -2×10^{-11} 1/m/s.

[49] It is evident that QTDWs are only observed above these jet instability regions that descend in altitude with time (see Figure 4, upper row). Also the temporal substructure of the QTDW bursts seems to be related to the substructure of the jet instability regions. Furthermore, it is noteworthy that main QTDW activity occurs shortly after the peak wind speeds in the instability regions, and not during the whole period of jet instability. Obviously, also the strength of the wind jet or other factors are likely important for details of the forcing of QTDWs.

[50] It should also be mentioned that the summertime westward wind jet is tilted and descends in altitude with time. Similar as for the QBO in the stratosphere, this indicates that the deceleration of the wind jet is likely caused by atmospheric waves, in particular GWs. This is further supported by the distribution of GW momentum flux shown in Figure 4, middle row. High momentum flux values are also tilted and descend with time, following the shape of the summertime westward jet. Thereby they form typical triangular shapes similar to the ones found, for example, by *Ern and Preusse* [2009a] for momentum fluxes of Kelvin waves interacting with the QBO winds.

[51] This tilted shape is also reflected in the distribution of GW drag shown in Figure 4, lower row. High values of GW drag are found on top of the summertime westward jets and descend in altitude with time. This is strong evidence that this GW drag is very likely opposite to the prevailing wind speed and contributes to the deceleration of the westward wind jet, starting shortly after peak wind speeds. There seems to be a close relationship between the jet instability regions (magenta hatched areas) and enhanced GW drag. High values of GW drag are found always directly above the instability regions and descend in altitude with time together with those regions. This enhanced GW drag decelerates the zonal wind directly above the instability regions and in this way contributes significantly to the vertical curvature of the jet that causes the jet instability. This means that GWs are directly involved in the forcing of QTDWs. Furthermore, core regions of QTDW forcing seem to be located at about 60 km altitude and 30° latitude.

[52] The timing of the QTDW bursts in these core regions is investigated in more detail in Figure 5. The upper row shows QTDW temperature amplitudes for zonal wavenumbers 3 (black solid lines) and 4 (black dashed lines) in degrees Kelvin (y-axis to the left). Overplotted are the zonal mean quasi-geostrophic zonal wind in m/s (blue lines, y-axis to the right), and $\partial\bar{Q}/\partial y$ in 10^{-12} 1/m/s (red dashed lines, y-axis to the right). In the lower row of Figure 5 GW drag in m/s/day (red lines, y-axis to the left), and GW momentum flux in 10^{-3} Pa (blue lines, y-axis to the right) are given. The left (right) column is for the Southern (Northern) Hemisphere. All values given are averages over 10 years of SABER data from 2002 until 2011. The time scales (x-axes) represent day numbers of the average year. For the Southern Hemisphere values are partly negative to indicate the change of the year during the time period shown. From Figure 5 it can be seen that, also in a more climatological sense, QTDWs are forced during periods of $\partial\bar{Q}/\partial y < 0$ shortly after maximum wind speeds and maximum GW momentum fluxes when the westward zonal wind jet starts to be decelerated. It is known from many modeling studies that GWs strongly contribute to this deceleration [e.g., *Holton*, 1982; *Holton*, 1983; *Pendlebury*, 2012], and this is also reflected in Figure 5, lower row, by increased GW drag values during the periods of jet attenuation.

3.1.2. QTDW Propagation Direction and Eliassen-Palm Fluxes

[53] To investigate the propagation direction of the QTDWs, we have estimated their vertical wavelength from vertical phase gradients. Positive values stand for phase fronts tilted westward with altitude, indicating upward propagation of the westward propagating QTDWs, while negative values stand for

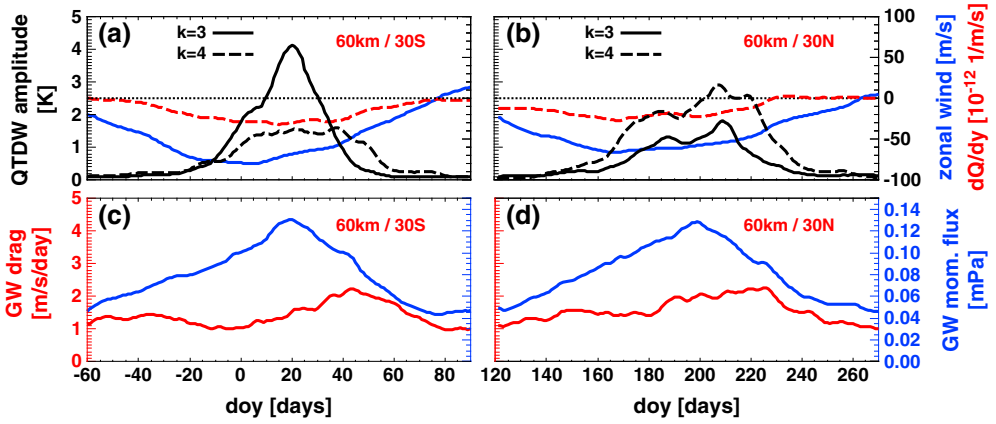

Figure 5. Temporal evolution of several parameters averaged over 10 years of SABER data (2002–2011) in the core region of QTDW forcing. Shown are values at 30°S and 60 km altitude (Southern Hemisphere) for the average period 1 November until 1 April (left column) and values at 30°N and 60 km altitude (Northern Hemisphere) for the average period 1 May until 28 September (right column). The upper row shows QTDW amplitudes in K for zonal wavenumbers $k=3$ (black solid) and $k=4$ (black dashed), scale on left y-axis, as well as mean quasi-geostrophic zonal wind in m/s (blue solid) and meridional gradients of the quasi-geostrophic zonal mean PV ($\partial\bar{Q}/\partial y$) in 10^{-12} 1/m/s (red dashed), scale on right y-axis. The lower row shows observed GW drag absolute values (red solid) in m/s/d (scale on left y-axis), as well as GW momentum flux absolute values (blue solid) in mPa (i.e., 10^{-3} Pa, scale on right y-axis).

eastward tilted phase fronts and downward propagation. Altitude-time cross-sections of these results are shown in Figure 6a for the QTDW of zonal wavenumber $k=3$ in the Southern Hemisphere, and in Figure 6b for $k=4$ in the Northern Hemisphere. Values are only shown for QTDW amplitudes exceeding an amplitude threshold, which is 0.5 K at 50 km altitude and increases linearly with altitude until reaching 2.5 K at 100 km. Latitudes and time periods are the same as in Figure 4, and like in Figure 4 zonal wind values are overplotted as white contour lines, and regions of strong jet instability ($\partial\bar{Q}/\partial y < -2\times10^{-11}$ 1/m/s) are indicated by hatched areas bounded by magenta contour lines.

[54] We find strongly positive vertical wavelengths of about 60 km in the jet instability regions and above, while directly below these regions vertical wavelengths are strongly negative. This can be clearly seen in Figure 6a and is only weakly indicated in Figure 6b. This characteristic is even more evident in the multiyear averages presented in Figure 9 (see section 3.2). Obviously QTDWs propagate upward above the instability regions, and downward below. This is in good agreement with *Limpasuvan and Wu* [2003] who found that the energy flux of QTDWs is directed upward, and supports the theory that QTDWs are indeed generated in those regions of strong jet curvature.

[55] To investigate the effect of QTDWs on the background circulation, we have estimated the Eliassen-Palm flux (EP flux) from SABER observations. For this purpose, we have calculated longitude-time spectra for SABER geopotential height observations in the same way as described before for temperatures (see section 2.2.1). Again, only the spectrum of westward-propagating waves with frequencies between 0.3 and 0.7 cycles/d is used to calculate daily global maps of geopotential height perturbations due to QTDWs. Similar as in section 2.4 geopotential height is converted to geopotential, and, based on the quasi-geostrophic assumption, zonal and meridional wind perturbations due to the QTDWs are estimated from global maps of geopotential and attributed to different QTDW zonal wavenumbers by Fourier analysis.

[56] Following *Andrews et al.* [1987] the EP flux of resolved waves (in our case QTDWs) on log-pressure levels is defined as follows using spherical coordinates:

$$F^{(\Phi)} = \rho_0 a\cos\Phi\left(\frac{\overline{v'\Theta'}}{\bar{\Theta}_z}\bar{u}_z - \overline{u'v'}\right) \tag{8}$$

$$F^{(z)} = \rho_0 a\cos\Phi\left[\left(f - \frac{(\bar{u}\cos\Phi)_\Phi}{a\cos\Phi}\right)\frac{\overline{v'\Theta'}}{\bar{\Theta}_z} - \overline{u'w'}\right] \tag{9}$$

with $F^{(\Phi)}$ the meridional and $F^{(z)}$ the vertical component of EP flux, ρ_0 the density of the background atmosphere, a the Earth radius, Φ the latitude, f the Coriolis frequency, $\bar{u}$ the zonal-mean zonal background wind, u', v', and w' the zonal, meridional, and vertical wind perturbations due to (resolved) waves, Θ' the potential temperature perturbation due to (resolved) waves, and $\bar{\Theta}$ the zonal-mean background potential temperature. Subscripts Φ and z denote differentiation by latitude and log-pressure height, respectively. Overbars indicate zonal averaging. The only quantity that is not available from SABER observations is w'. Therefore, the term $u'w'$ in equation (9) has been neglected.

[57] The EP flux divergence ∇F is given by

$$\nabla F = \frac{1}{a\cos\Phi}\frac{\partial}{\partial\Phi}\left(F^{(\Phi)}\cos\Phi\right) + \frac{\partial}{\partial z}F^{(z)} \tag{10}$$

and the zonal wind tendency $\bar{X}_{\mathrm{res}}$ caused by wave drag of resolved waves (in our case QTDW drag) is given by

$$\bar{X}_{\mathrm{res}} = \frac{1}{\rho_0 a\cos\Phi}\nabla F \tag{11}$$

[58] See also *Andrews et al.* [1987].

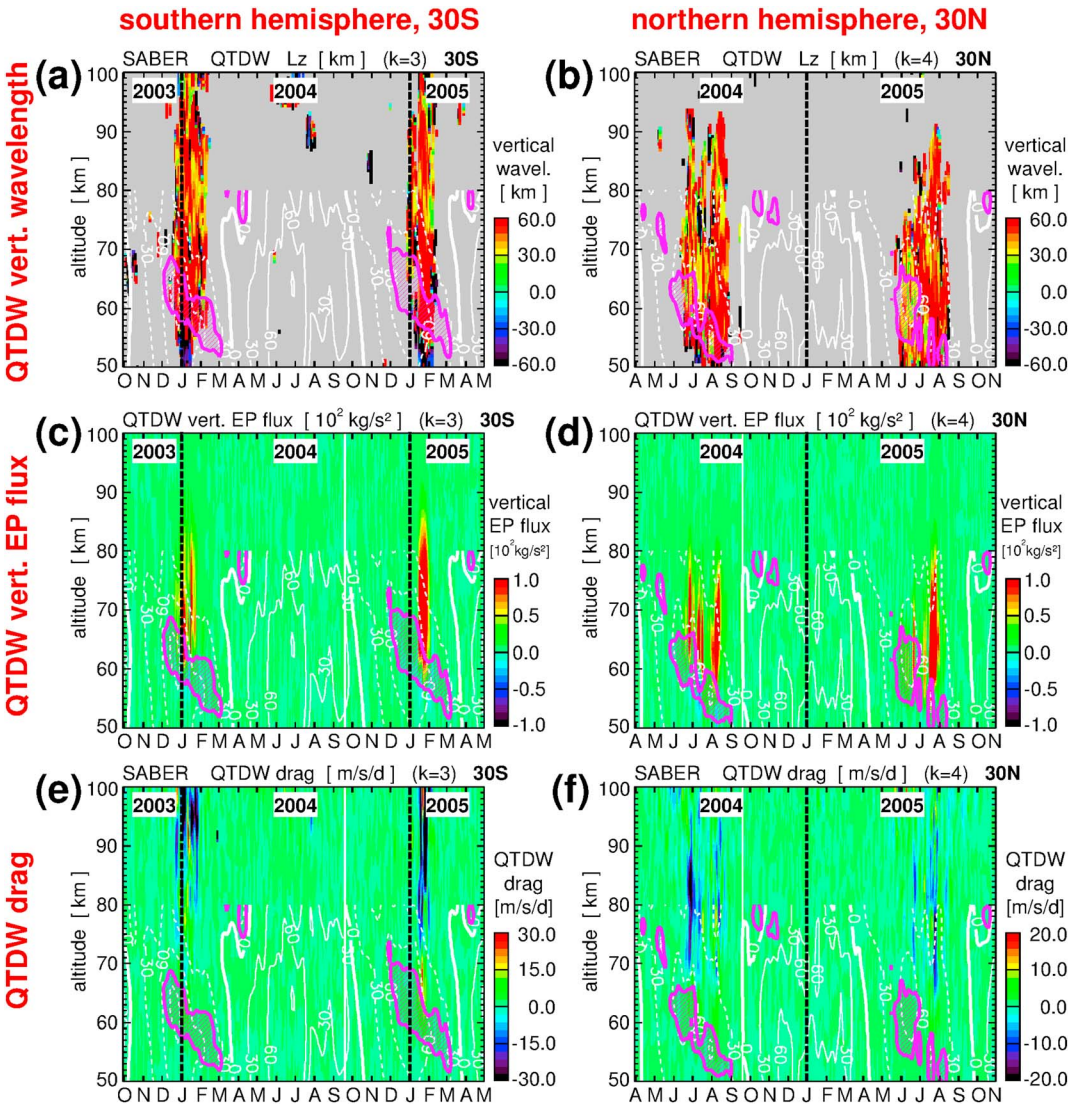

Figure 6. Same as Figure 4, but shown are for the QTDW with zonal wavenumber $k=3$ in the Southern Hemisphere (a) vertical wavelength, (c) vertical EP flux, and (e) wave drag calculated from the EP flux divergence. (b), (d), and (f) Same, but for the $k=4$ QTDW in the Northern Hemisphere.

[59] Values of vertical EP fluxes due to QTDWs with zonal wavenumber $k=3$ in the Southern Hemisphere at 30°S are shown in Figure 6c. Figure 6d shows the same, but for $k=4$ at 30°N in the Northern Hemisphere. We find high values of upward directed EP flux directly above the jet instability regions. As expected, the temporal variations of EP flux closely follow the temporal variability of QTDW activity (see Figure 4). In the upper mesosphere vertical EP flux strongly decreases because of the enhanced dissipation of QTDWs at high altitudes.

[60] Also, QTDW drag from the divergence of EP flux (see equations (10) and (11)) has been calculated and is presented in Figures 6e and 6f. QTDW drag is strongly intermittent in time and mostly directed westward in the upper mesosphere and lower thermosphere. For short periods of enhanced wave drag values as strong as –30 m/s/d and even stronger can be found. It looks like the $k=3$ QTDW in the Southern Hemisphere exerts stronger drag on the background wind than the $k=4$ QTDW in the Northern Hemisphere. Furthermore, the $k=4$ QTDW in the Northern Hemisphere seems to dissipate at lower altitudes and enhanced values of QTDW drag are more confined to the upper mesosphere (altitudes below about 90 km), while the $k=3$ QTDW in the Southern Hemisphere also exerts strong drag in the lower thermosphere (at altitudes around 100 km and above). This is also reflected in the reduction of QTDW amplitudes of the $k=4$ QTDW already in the upper mesosphere (see Figures 4a and 4b). It also seems that QTDW drag in both Southern and Northern hemispheres can be directed slightly eastward in the lower mesosphere. This will be discussed in more detail in section 3.2.

3.2. Zonal Cross-Sections Averaged Over all Periods of Strong QTDW Activity in the Years 2002–2011

[61] Altitude-time cross-sections as discussed in section 3.1 have given some first information about the QTDW forcing mechanism. For a better understanding and a full three-dimensional view, however, also zonal cross-sections of all parameters have to be considered. For this purpose, we have averaged zonal averages of zonal winds, QTDW

amplitudes, GW momentum flux, GW drag, QTDW vertical wavelengths, QTDW EP fluxes, QTDW drag, and $\partial\bar{Q}/\partial y$ over all periods of strong QTDW bursts, separately for the Southern and the Northern hemispheres. A QTDW burst has been assumed to be strong in all cases when QTDW amplitudes of either zonal wavenumber 3 or 4 exceed a threshold value of 2 K at 70 km altitude and 34° latitude in the respective hemisphere.

[62] The results of this procedure are shown in Figures 7 and 9. In each panel the left half represents Southern Hemisphere summertime conditions during strong QTDW activity in the Southern Hemisphere, while the right half of each panel is representative of Northern Hemisphere summer conditions during strong QTDW activity in the Northern Hemisphere. Furthermore, it should be mentioned that only latitudes equatorward of 50° are continuously covered by SABER observations. Therefore, all parameters will show discontinuities (jumps) at about 50° latitude.

3.2.1. Background Wind and QTDW Amplitudes

[63] Figure 7a shows zonal winds averaged as described above. The mesospheric summertime westward jets display the well-known structure with their poleward tilted shape. It is also well known that in the lower mesosphere this jet is somewhat weaker in the Northern Hemisphere compared to the Southern Hemisphere. The jump in wind speeds at 50° latitude is caused by the reduced temporal coverage of high latitudes due to the yaw cycles of the TIMED satellite. These higher latitudes are however not relevant for our study because of the low QTDW amplitudes at high latitudes in the altitude range considered.

[64] In Figure 7b averaged values of $\partial\bar{Q}/\partial y$ are shown. The regions of $\partial\bar{Q}/\partial y < 0$, indicative of jet instabilities and regions of possible QTDW forcing, are sloped with latitude and altitude and follow the shape of the zonal wind jets. As we have seen in section 3.1 the jet instability seems to be seeded by GW drag close to the upper part of those regions. In both hemispheres this upper part coincides roughly with a sloped straight line between about 15° latitude/45 km altitude and 45° latitude/75 km altitude, and flattening somewhat toward even higher latitudes. For comparison, these lines have been added in all panels of Figure 7. Furthermore, in Figures 7c–7f white contour lines represent the zonal wind shown in Figure 7a. Contour increment is 30 m/s. Westward wind is indicated by dashed contour lines. The magenta contour line also given in Figures 7c–7f indicates the value of $\partial\bar{Q}/\partial y = -0.15 \times 10^{-10}$ 1/m/s to highlight the possible forcing regions of QTDWs.

[65] Figures 7c and 7d show average amplitudes for QTDWs with zonal wavenumber 3 and 4, respectively. It is evident that also in these latitude-altitude cross-sections the onset of high QTDW amplitudes closely follows the areas of especially strong jet instabilities bounded by the magenta contour lines. This is further strong evidence that, indeed, QTDWs are excited by instabilities of the zonal wind jets.

3.2.2. GW Momentum Flux and GW Drag

[66] To study the role of GWs in the forcing of QTDWs, Figure 7e shows average zonal cross-sections of GW momentum flux. It is striking that enhanced GW momentum fluxes closely follow the upper edge of the QTDW source regions. These enhancements of GW momentum flux have been attributed to GWs generated by deep convection that propagate upward and poleward, starting from their source regions in the summertime subtropics [*Preusse et al.*, 2009b; *Ern et al.*, 2011] (as mentioned above, also GWs generated at middle latitudes might contribute to some extent). Obviously the jet instabilities that are responsible for the forcing of QTDWs are seeded along the propagation pathway of those convectively generated GWs.

[67] This is further confirmed by the average GW drag shown in Figure 7f (regions with values below 0.3 m/s/d and regions not covered with data are left blank). Enhanced GW drag is found directly above the jet instability regions, and obviously the curvature of the zonal wind jet is seeded by the breaking of the abovementioned GWs. It should also be noted that the observed GW drag enhancements are always found directly above and equatorward of the tilted jet instability regions. This means that, by deceleration of the zonal wind jet, GW drag will likely not only contribute to the vertical, but also to the meridional curvature of the jet.

[68] This characteristic distribution of enhanced GW drag at the upper edge of the jet instability regions of the summertime mesospheric wind jets is very similar to the model simulations by *Pendlebury* [2012] with weaker GW drag at low latitudes and stronger drag toward high latitudes. The direction of GW drag in *Pendlebury* [2012] is eastward, which further supports our assumption that also our observed GW drag is directed opposite to the strong wind jet. Also, *Pendlebury* [2012] attributes the formation of the jet instability region to the curvature of the jet introduced by this GW drag. The main difference between *Pendlebury* [2012] and our study is that peak values by *Pendlebury* [2012] are about 20 m/s/d at low latitudes and well above 100 m/s/d at high latitudes, while our peak values are somewhat lower (about 5 and 100 m/s/d, respectively). This can however easily be explained by the fact that SABER observes only a part of the GW spectrum and will therefore underestimate the total GW drag present in the atmosphere.

3.2.3. Zonal Distribution of Gravity Waves in the Jet Instability Regions

[69] It is well known from observations [e.g., *Jiang et al.*, 2004; *Ern et al.*, 2004, 2011; *Wright and Gille*, 2011; *Ern and Preusse*, 2012], as well as modeling studies [e.g., *Beres*, 2005; *Choi et al.*, 2012] that the distribution of GWs in the summertime subtropics displays a characteristic longitudinal structure that is governed by GWs generated by deep convection. Please note that this structure is not a consequence of GW modulation by QTDWs: The longitudinal variation is already seen in the lower stratosphere [*Ern and Preusse*, 2012], i.e., directly above the GW sources, where no QTDW activity is observed. Furthermore, periods of enhanced GW activity in the summertime subtropics have a longer duration than the short bursts of QTDW activity (see also Figures 3, 4, and 5). Because longitudinally varying GW drag can excite global-scale waves [e.g., *Holton*, 1984; *Meyer*, 1999], it has been speculated by *Limpasuvan and Wu* [2003] that this effect could directly be involved in the forcing of QTDWs.

[70] In the following, the zonal GW distribution along the sloped lines marking the seeding region of jet curvature in Figure 7 is investigated. Again, average distributions are calculated from all times of strong QTDW bursts in the years

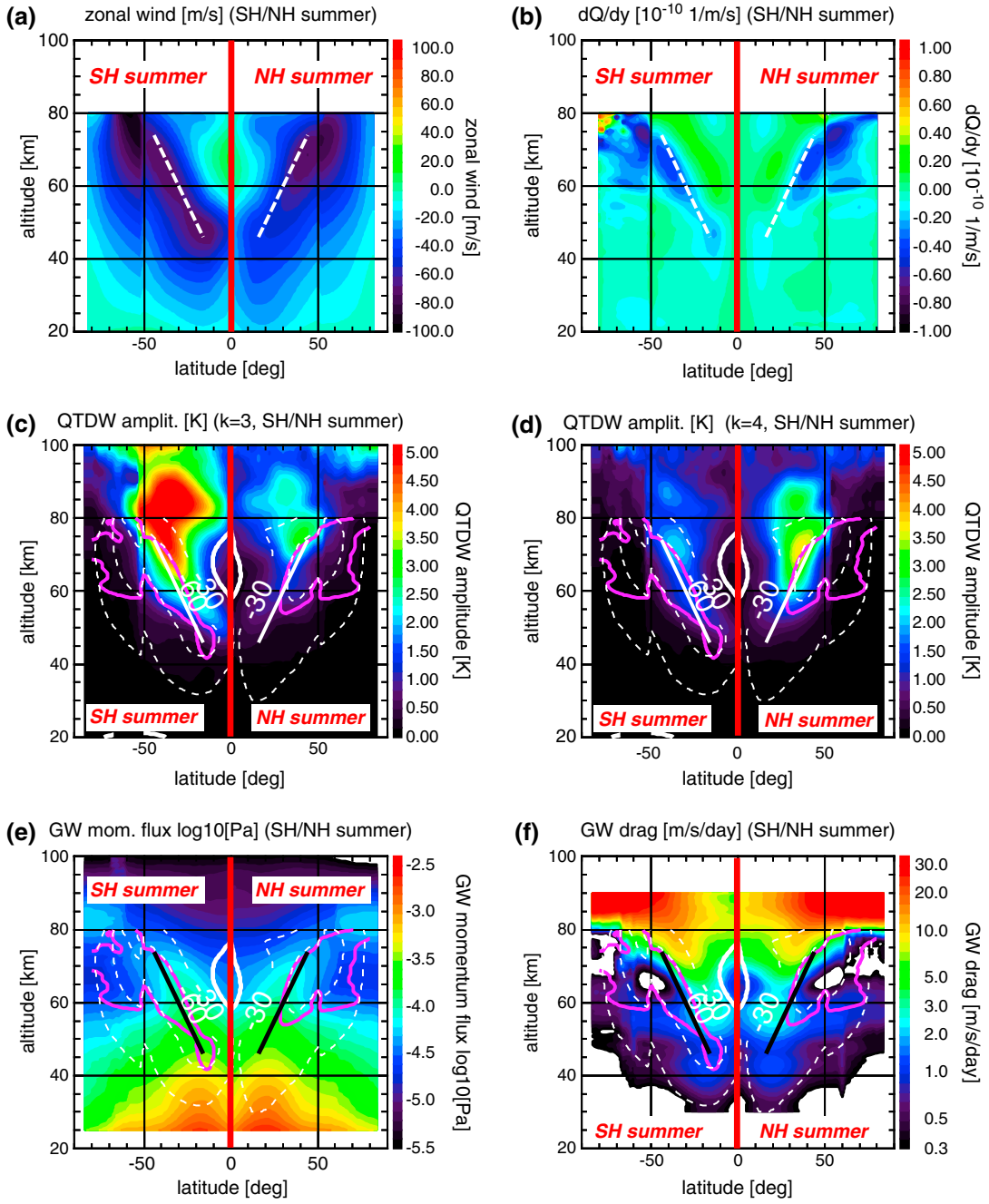

Figure 7. Zonal mean cross-sections averaged over periods of strong QTDW activity in 10 years of SABER data (2002–2011), separately for the Southern (left half of each panel) and the Northern hemispheres (right half of each panel). Shown are (a) zonal mean quasi-geostrophic wind in m/s, (b) meridional gradients of quasi-geostrophic zonal mean PV ($\partial\bar{Q}/\partial y$) in 10^{-10} 1/m/s, (c) QTDW amplitudes in K for zonal wavenumbers $k=3$, and (d) $k=4$, (e) GW momentum flux in $\log_{10}$(Pa), and (f) GW drag in m/s/d. White contour lines in Figures 7c–7f represent the zonal winds from Figure 7a in m/s. Contour increment is 30 m/s, dashed lines indicate westward wind. The magenta contour lines in Figures 7c–7f represent the value of $\partial\bar{Q}/\partial y = -1.5 \times 10^{-11}$ 1/m/s, taken from Figure 7b. In all panels bold lines sloped with latitude and altitude indicate regions where GW drag likely seeds jet instabilities ($\partial\bar{Q}/\partial y < 0$).

2002–2011. Figure 8a shows the average zonal distribution of GW momentum flux. In Figure 8a different latitudes also represent different altitudes because the distributions shown are on sloped sections, following the sloped lines given in Figure 7. Nevertheless, the longitudinal variation in both Southern and Northern hemispheres is found to be consistent at all latitudes (altitudes). This is another indication that the GWs seen along those latitude/altitude sections are from about the same source regions in the troposphere. Please note that also in the simulation by *Beres* [2005] the longitudinal pattern caused by the tropospheric sources is still preserved in the mesopause region.

[71] For the distributions shown in Figure 8a we now average the values in latitude/altitude over the whole section to highlight the longitudinal structure. The results are presented in Figure 8b. The black (red) solid line shows average momentum fluxes for Southern (Northern) Hemisphere summer during strong QTDW activity. Indeed, we find a characteristic longitudinal variation of GW momentum flux. Spectral amplitudes obtained by Fourier analysis of the data presented in Figure 8b are shown in Figure 8c. The spectral decomposition displays significant amplitudes for zonal wavenumbers 1–4 in both hemispheres with maximum amplitude at wavenumbers 2 or 3. Longitudinal variations of GW drag are very similar (not shown). The most dominant QTDW modes are zonal wavenumbers 3 and 4, and there is also significant spectral power in the longitudinal distribution of GWs at these wavenumbers. This indicates that GWs have the potential to force these QTDW modes.

[72] The spectra shown in Figure 8c are however not "monochromatic" and always contain significant contributions of several zonal wavenumbers. Therefore, it is not clear how the longitudinal structure in GW drag might be directly linked to the "selection" of the excited QTDW modes, as well as to their relative strength. Obviously, this approach is too simple, and the forcing of QTDWs is also influenced by other factors, for example the strength of the zonal wind jet or diurnal variations of the GW sources (e.g., deep convection). Also, tides could be involved in the generation of QTDWs. This has been indicated by several studies, for example, *Salby and Callaghan* [2008], *McCormack et al*. [2010], or *Hecht et al*. [2010]. Further investigation of these complicated processes is however beyond the scope of our current work and will also require modeling approaches.

3.2.4. QTDW Propagation Direction, EP Fluxes, and EP Flux Divergence

[73] In Figures 9a and 9b also zonal cross-sections of QTDW vertical wavelengths for zonal wavenumbers $k=3$ (Figure 9a) and $k=4$ (Figure 9b) are investigated in multiyear averages over periods of strong QTDW activity, as defined above. Like in Figure 6 values of vertical wavelengths are only used when the QTDW amplitude exceeds a threshold value. Similar as in Figures 6a and 6b we find that on average the vertical wavelength is positive above the jet instability regions, and negative below, for both zonal wavenumbers 3 and 4. Again, this indicates that QTDWs propagate upward above the instability regions, and downward below.

[74] Multiyear averages of meridional and vertical EP fluxes summarized over QTDWs with zonal wavenumber 3 and 4 are presented in Figures 9c and 9d, respectively. Meridional EP flux is directed strongly equatorward at low altitudes (around 60 km) and low latitudes (between about 10° and 30° of the respective hemisphere). At higher altitudes (around 80 km) and somewhat higher latitudes (poleward of about 20°–30°) meridional EP flux is directed poleward. We find positive values of vertical EP flux above the jet instability regions, and slightly negative values below. This is further illustrated by the EP flux vectors that are overplotted in Figures 9c and 9d. Please note that in Figure 9d the negative part of the color scale is stretched to emphasize these negative values. Similarly, negative y-coordinates of the EP flux vectors are exaggerated by a factor of two, if applicable, to emphasize regions of downward flux.

[75] The orientation of the EP fluxes is qualitatively in good agreement with the modeling study by *Pendlebury* [2012], Figure 6. Some minor differences may arise because *Pendlebury* [2012] investigates the short-term temporal evolution of QTDWs and distinguishes between growing and mature phases of QTDW activity, and our multiyear averages will be a mixture of both stages.

[76] Comparison with QTDW EP flux observations by *Lieberman* [1999, 2002] also shows qualitative agreement. In this study [see *Lieberman*, 2002, Figure 1] vertical EP flux is mainly directed upward (only altitudes above 65 km are shown), while meridional EP flux is mainly equatorward at low altitudes and low latitudes, and poleward at higher altitudes and higher latitudes. The pattern is somewhat different from our results. This could however be an effect of interannual variability, because the study by *Lieberman* [1999, 2002] covers only a short period of 12 days in January 1994.

[77] Multiyear averages of the QTDW drag exerted on the background zonal wind are shown in Figure 9e for zonal wavenumber 3, and in Figure 9f for zonal wavenumber 4. This time, the positive part of the color scale has been stretched to emphasize small values of positive QTDW drag. We find strongly negative (=westward) QTDW drag at high altitudes (above the jet instability regions) in the latitude range between about 20° and 60° in the respective hemisphere. This means that QTDWs redistribute westward momentum from lower to higher altitudes while they propagate upward, and at higher altitudes QTDW drag counteracts the summertime wind reversal from westward wind in the mesosphere to eastward wind in the upper mesosphere and lower thermosphere. For this well-known wind reversal to develop, the westward directed QTDW drag has to be overcompensated by eastward-directed GW drag, drag exerted by other global scale waves (e.g., tides), and meridional and vertical advection terms of the background atmosphere. On average, the QTDW drag is dominated by the strongest QTDW mode in the respective hemisphere: by zonal wavenumber $k=3$ in the Southern Hemisphere, and by $k=4$ in the Northern Hemisphere. As already mentioned before, this strong westward QTDW drag is found at higher altitudes for zonal wavenumber 3 (above 80 km) than for zonal wavenumber 4. This is the case because QTDWs with zonal wavenumber 4 start to dissipate already at somewhat lower altitudes. Furthermore, QTDW drag is considerably stronger on average in the Southern Hemisphere (please note the different ranges of the color scales in Figures 9e and 9f). One striking feature are positive (=eastward) values of QTDW drag in the core of the mesospheric westward zonal wind jets where the jet instability regions are located.

[78] Again, these results are in good qualitative agreement with the modeling study by *Pendlebury* [2012]. In particular, *Pendlebury* [2012] also finds regions of eastward QTDW drag in the jet instability regions, and it is pointed out that this effect may be related to the process of wave generation. One main difference between *Pendlebury* [2012] and our study is that our peak values of QTDW drag (about 30 m/s/d) are considerably lower than the ones in *Pendlebury* [2012] (about two times higher). Possible reasons could be that our values are averages containing also periods of weaker QTDW activity, while the values in *Pendlebury* [2012] are representative for 5 day periods only. Furthermore, it should be noted that *Pendlebury* [2012] is only a modeling study that may not be

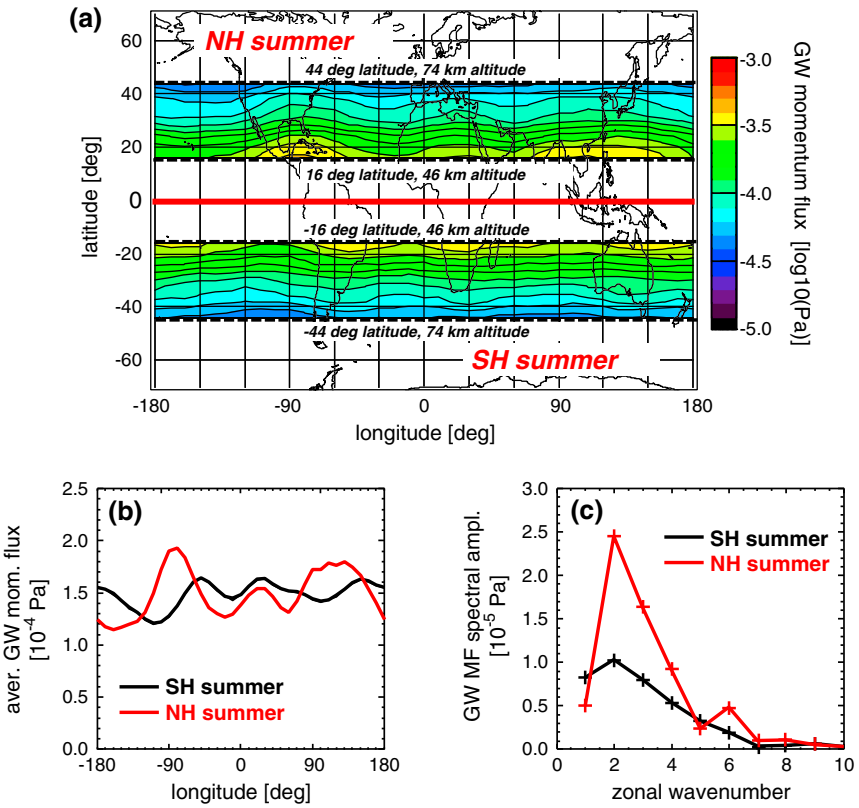

Figure 8. Shown is (a) the distribution of gravity wave momentum flux absolute values in log_{10}(Pa) along the latitude-altitude sections, as defined by the bold lines in Figure 7. Values are averages over all periods of strong QTDW activity in the years 2002–2011, determined separately for the Southern and the Northern hemispheres. (b) The zonal distribution of SABER GW momentum flux absolute values in 10^{-4} Pa meridionally averaged over the global distributions shown in Figure 8a. (c) The zonal wavenumber spectrum (spectral amplitudes) of the distributions shown in Figure 8b. In Figures 8b and 8c, values are given separately for the Southern (black solid) and the Northern hemispheres (red solid).

fully realistic in all aspects. Another difference in *Pendlebury* [2012] is enhanced values of QTDW drag close to the equator that can occur during the mature phase of a QTDW burst in some years. This effect is also seen in our QTDW drag distributions (not shown), but is averaged out in our multiyear averages.

[79] Comparison with the observational study by *Lieberman* [1999, 2002] on the other hand shows good qualitative agreement in the peak values of QTDW drag (about 40 m/s/d in Figure 1 of *Lieberman* [2002]). However, the global pattern is somewhat different. Again, this could be an effect of interannual variability and the short time period that is only covered by *Lieberman* [1999, 2002].

4. Summary and Discussion

[80] Quasi two-day wave (QTDW) amplitudes have been derived from both HIRDLS and SABER temperature observations in the mesosphere. In addition, QTDW vertical wavelengths, EP fluxes and EP flux divergence (QTDW drag) have been estimated from SABER temperatures and geopotential heights. We find very good agreement between HIRDLS and SABER QTDW amplitudes on one hand, and between SABER and an independent analysis by *Tunbridge et al*. [2011] based on MLS/Aura temperatures, on the other hand. In particular, from SABER observations in the years 2002–2011, a 10 year climatology of QTDW amplitudes has been derived that covers the whole mesosphere and also the lower thermosphere. This climatology is compared with quasi-geostrophic winds, as well as gravity wave (GW) momentum flux absolute values and GW drag absolute values, derived also from SABER temperature observations. Furthermore, meridional gradients of the zonal mean quasi-geostrophic potential vorticity ($\partial\bar{Q}/\partial y$) have been calculated. Negative values of $\partial\bar{Q}/\partial y$ indicate regions of zonal wind jet instabilities that are believed to be responsible for the forcing (i.e., generation and/or amplification) of QTDWs [e.g., *Plumb*, 1983; *Pfister*, 1985; *Norton and Thuburn*, 1996; *Salby and Callaghan*, 2001; *Rojas and Norton*, 2007].

[81] The strongest QTWD activity in the mesosphere is observed between about 20° and 40° latitude. We find that QTDW activity is closely linked to instability regions of the summertime mesospheric westward zonal wind jet. Core regions of QTDW forcing are located around 30° latitude and 60 km altitude. QTDWs are mainly observed above the regions of jet instability, and the vertical phase tilt of the QTDWs indicates that they propagate upward above and downward below the jet instabilities. This is a clear evidence that QTDWs are indeed forced by those jet instabilities. However, QTDWs are not observed during the whole period

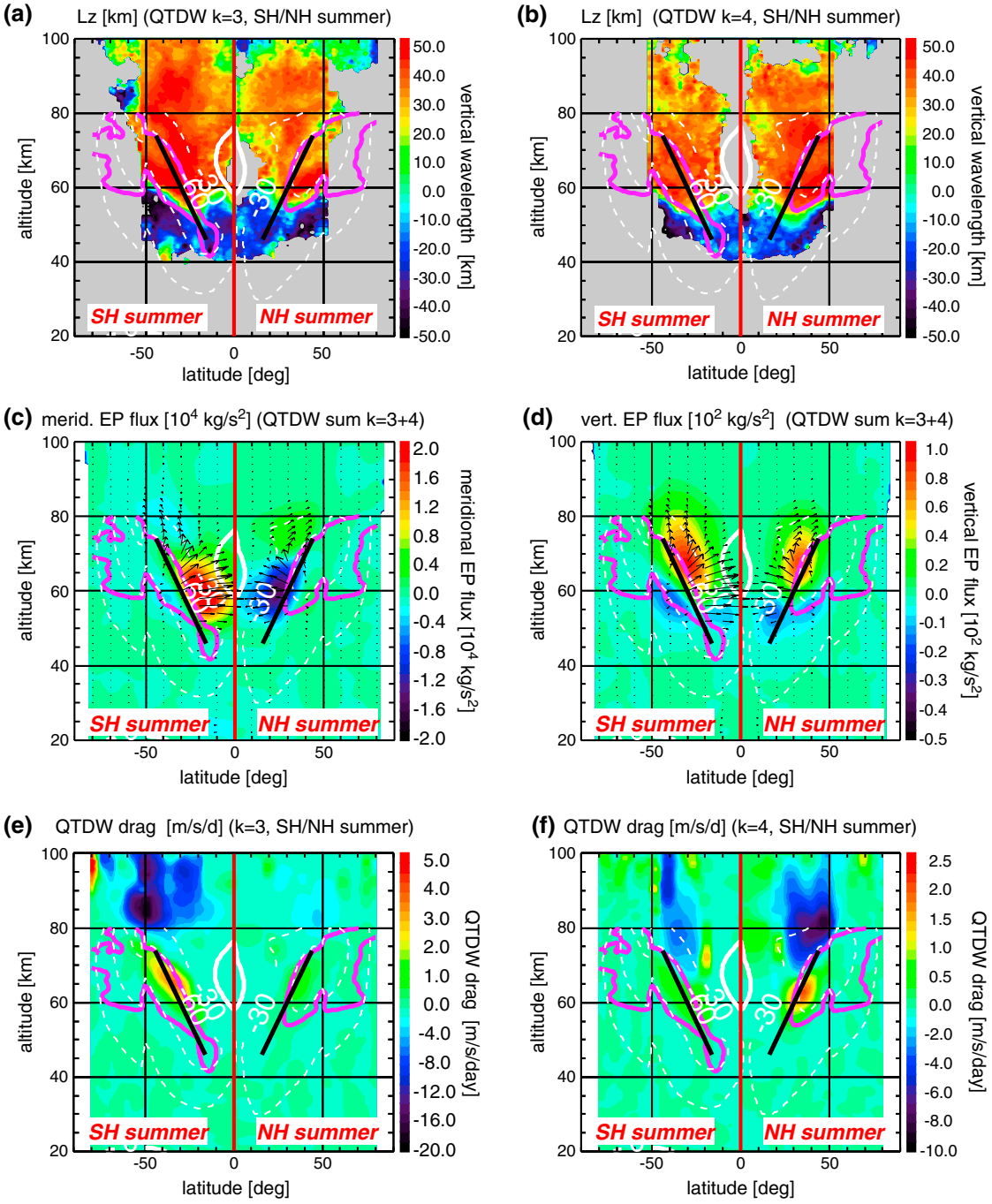

Figure 9. Same as Figure 7, but shown are the vertical wavelength for QTDWs with zonal wavenumber (a) $k=3$ and (b) $k=4$. Also shown are (c) the meridional and (d) the vertical EP flux, both summarized over QTDWs with zonal wavenumbers $k=3$ and $k=4$. Overplotted in Figures 9c and 9d are the EP flux vectors obtained by combining the meridional and vertical fluxes from Figures 9c and 9d. To emphasize regions of downward flux, negative y-coordinates of the arrows are exaggerated by a factor of two, if applicable. In Figures 9e and 9f the QTDW wave drag resulting from the EP flux divergence is given for (e) $k=3$ and (f) $k=4$. Please note that in Figures 9d, 9e, and 9f positive and negative parts of the color scale are scaled differently.

of jet instability. This indicates that also other factors will play an important role.

[82] It is remarkable, that enhancements of observed GW drag are closely linked to the jet instability regions. GW drag is enhanced directly above and directly equatorward of the instability regions. Furthermore, GW drag enhancements descend in altitude with time together with the instability regions when the summertime mesospheric jet weakens and also descends in altitude with time. This means that this GW drag is very likely directed opposite to the summertime

mesospheric wind jet, and, by decelerating the zonal wind jets, it likely seeds the curvature of the zonal wind jets that is responsible for the regions of jet instability. These findings are in remarkable agreement with a modeling study by *Pendlebury* [2012].

[83] We have determined the EP fluxes of the QTDWs from SABER observations, as well as the resulting EP flux divergence (QTDW drag). Vertical EP flux is directed strongly upward above the jet instability regions, and slightly downward below. Meridional EP flux is directed strongly equatorward at low altitudes (around 60 km) and low latitudes (about 10°–30° in the respective hemisphere). At higher altitudes (~80 km) and somewhat higher latitudes (poleward of about 20°–30°) meridional EP flux is directed poleward. We find strong westward QTDW drag at high altitudes and latitudes between about 20° and 60° in the respective summer hemisphere, i.e., above the jet instability regions. Peak values are about 30 m/s/d westward. On average, the QTDW drag is dominated by zonal wavenumber 3 in the Southern, and wavenumber 4 in the Northern Hemisphere. In the Southern Hemisphere QTDW drag is considerably stronger. Strikingly, we find that QTDW drag is eastward in the core of the mesospheric westward zonal wind jets where the jet instability regions are located. This means that QTDWs have a weakening effect on the westward jet in its core, and they counteract the wind reversal in the upper mesosphere. Again, all these results are in remarkable agreement with the model study by *Pendlebury* [2012], and, as pointed out by *Pendlebury* [2012], eastward values of QTDW drag in the jet instability regions could be an indication of wave generation processes. There is also good qualitative agreement with previous observations of QTDW EP fluxes and EP flux divergence by *Lieberman* [1999, 2002].

[84] The jet instability regions are tilted in latitude and altitude, and, remarkably, they coincide with regions where a mixture of GWs generated during summertime at middle latitudes and in the subtropics exhibits a characteristic longitudinal structure. In particular, the meridional propagation of GWs generated in the summertime subtropics (mostly in the monsoon regions) will play an important role. This longitudinal structure is persistently found along the latitudes and altitudes of jet instability. This finding supports considerations by, for example, *Limpasuvan and Wu* [2003] or *Ern et al.* [2011] that nonuniformities in the zonal distribution of GWs could directly be responsible for the generation of QTDWs.

[85] We have analyzed the zonal distribution of GWs at the top of the jet instability regions. However, a clear relationship between dominant zonal wavenumbers of the zonal distribution of GWs and observed QTDW zonal wavenumbers is not found. It should be mentioned that, of course, for the generation of travelling planetary waves a fixed zonal distribution of GW drag is likely not sufficient, and it can be speculated that also temporal variations of GW drag introduced by, for example, the diurnal cycle of deep convection in the summertime subtropics might be important. Several studies indicate that also tides might play an important role [e.g., *Salby and Callaghan*, 2008; *Hecht et al.*, 2010; *McCormack et al.*, 2010]. Furthermore, the strength of the zonal wind jets will also have an effect in the forcing of QTDWs and on the zonal wavenumbers observed.

[86] The current study is based completely on observations of the satellite instruments HIRDLS and, in particular, SABER. From these observations all required parameters have been derived: QTDW amplitudes, EP fluxes, EP flux divergence (QTDW drag), quasi-geostrophic winds, and GW momentum fluxes and GW drag. Even though derived quasi-geostrophic winds may be somewhat high-biased, and even though GW momentum fluxes and GW drag have large uncertainties and are representative only for part of the whole GW spectrum, all derived parameters give a very consistent picture of the mesospheric dynamics involved in the excitation of QTDWs. The results presented are therefore a good basis for modeling studies that may provide a more in-depth understanding of all processes contributing to QTDW forcing.

[87] **Acknowledgments.** The work of M. Ern was partly supported by Deutsche Forschungsgemeinschaft (DFG) grant no. ER 474/2–1 (GW-EXCITES) within the DFG priority program CAWSES (SPP–1176). SABER data were provided by GATS Inc., and HIRDLS data by NASA. Many thanks also go to the teams of the HIRDLS and SABER instruments for their continued effort. Very helpful comments by three anonymous reviewers are gratefully acknowledged.

References

Alexander, M. J., et al. (2010), Recent developments in gravity-wave effects in climate models and the global distribution of gravity-wave momentum flux from observations and models, *Q. J. R. Meteorol. Soc.*, *136*, 1103–1124, doi:10.1002/qj.637.

Altadill, D., J. G. Solé, and E. M. Apostolov (1998), First observation of quasi-2-day oscillations in ionospheric plasma frequencies at fixed heights, *Ann. Geophys.*, *16*, 609–617.

Andrews, D. G., J. R. Holton, and C. B. Leovy (1987), *Middle atmosphere dynamics*, 489 pp., Academic Press, Orlando, Fl.

Azeem, S. M. I., S. E. Palo, D. L. Wu, and L. Froidevaux (2001), Observations of the 2-day wave in UARS MLS temperature and ozone measurements, *Geophys. Res. Lett.*, *28*, 3147–3150.

Baldwin, M. P., L. J. Gray, T. J. Dunkerton, K. Hamilton, P. H. Haynes, W. J. Randel, J. R. Holton, M. J. Alexander, I. Hirota, T. Horinouchi, D. B. A. Jones, J. S. Kinnersley, C. Marquardt, K. Sato, and M. Takahashi (2001), The quasi-biennial oscillation, *Rev. Geophys.*, *39*, 179–229.

Becker, E., and D. C. Fritts (2006), Enhanced gravity-wave activity and interhemispheric coupling during the MaCWAVE/MIDAS northern summer program 2002, *Ann. Geophys.*, *24*, 1175–1188.

Beres, J. H. (2005), Estimates of mesospheric gravity wave activity over convection from a global model, *Adv. Space Res.*, *35*, 1933–1939, doi:10.1016/j.asr.2005.04.087.

Borries, C., N. Jakowski, Ch. Jacobi, P. Hoffmann, and A. Pogoreltsev (2007), Spectral analysis of planetary waves seen in ionospheric total electron content (TEC): First results using GPS differential TEC and stratospheric reanalyses, *J. Atmos. Sol. Terr. Phys.*, *69*, 2442–2451, doi:10.1016/j.jastp.2007.02.004.

Chang, L. C., J.-Y. Liu, and S. E. Palo (2011), Propagating planetary wave coupling in SABER MLT temperatures and GPS TEC during the 2005/2006 austral summer, *J. Geophys. Res.*, *116*, A10324, doi:10.1029/2011JA0166879.

Choi, H.–J., H.–Y. Chun, J. Gong, and D. L. Wu (2012), Comparison of gravity wave temperature variances from ray-based spectral parameterization of convective gravity wave drag with AIRS observations, *J. Geophys. Res.*, *117*, D05115, doi:10.1029/2011JD016900.

Dunkerton, T. J. (1997), The role of gravity waves in the quasi-biennial oscillation, *J. Geophys. Res.*, *102*, 26,053–26,076.

Ern, M., and P. Preusse (2009a), Wave fluxes of equatorial Kelvin waves and QBO zonal wind forcing derived from SABER and ECMWF temperature space-time spectra, *Atmos. Chem. Phys.*, *9*, 3957–3986, doi:10.5194/acp-9-3957-2009.

Ern, M., and P. Preusse (2009b), Quantification of the contribution of equatorial Kelvin waves to the QBO wind reversal in the stratosphere, *Geophys. Res. Lett.*, *36*, L21801, doi:10.1029/2009GL040493.

Ern, M., and P. Preusse (2012), Gravity wave momentum flux spectra observed from satellite in the summertime subtropics: Implications for global modeling, *Geophys. Res. Lett.*, *39*, L15810, doi:10.1029/2012GL052659.

Ern, M., P. Preusse, M. J. Alexander, and C. D. Warner (2004), Absolute values of gravity wave momentum flux derived from satellite data, *J. Geophys. Res.*, *109*, D20103, doi:10.1029/2004JD004752.

Ern, M., P. Preusse, and C. D. Warner (2006), Some experimental constraints for spectral parameters used in the Warner and McIntyre gravity wave parameterization scheme, *Atmos. Chem. Phys.*, *6*, 4361–4381, doi:10.5194/acp-6-4361-2006.

Ern, M., P. Preusse, M. Krebsbach, M. G. Mlynczak, and J. M. Russell III (2008), Equatorial wave analysis from SABER and ECMWF temperatures, *Atmos. Chem. Phys.*, *8*, 845–869, doi:10.5194/acp-8-845-2008.

Ern, M., C. Lehmann, M. Kaufmann, and M. Riese (2009), Spectral wave analysis at the mesopause from SCIAMACHY airglow data compared to SABER temperature spectra, *Ann. Geophys.*, *27*, 407–416.

Ern, M., P. Preusse, J. C. Gille, C. L. Hepplewhite, M. G. Mlynczak, J. M. Russell III, and M. Riese (2011), Implications for atmospheric dynamics derived from global observations of gravity wave momentum flux in stratosphere and mesosphere, *J. Geophys. Res.*, *116*, D19107, doi:10.1029/2011JD015821.

Fleming, E. L., S. Chandra, J. J. Barnett, and M. Corney (1990), Zonal mean temperature, pressure, zonal wind and geopotential height as functions of latitude, *Adv. Space Res.*, *10*, (12) 11–(12)59.

Forbes, J. M., and X. Zhang (1999), The quasi 2-day ionospheric oscillation: A statistical study, *J. Atmos. Sol. Terr. Phys.*, *59*, 1025–1034.

Forbes, J. M., S. L. Bruinsma, X. Zhang, and J. Oberheide (2009), Surface-exosphere coupling due to thermal tides, *Geophys. Res. Lett.*, *36*, L15812, doi:10.1029/2009GL038748.

Fritts, D. C., J. R. Isler, R. S. Lieberman, M. D. Burrage, D. R. Marsh, T. Nakamura, T. Tsuda, R. A. Vincent, and I. M. Reid (1999), Two-day wave structure and mean flow interactions observed by radar and High Resolution Doppler Imager, *J. Geophys. Res.*, *104*, 3953–3969.

Garcia, R. R., R. Lieberman, J. M. Russell III, and M. G. Mlynczak (2005), Large-scale waves in the mesosphere and lower thermosphere observed by SABER, *J. Atmos. Sci.*, *62*, 4384–4399.

Gille, J. C., J. J. Barnett, J. Whitney, M. Dials, D. Woodard, W. Rudolf, A. Lambert, and W. Mankin (2003), The High Resolution Dynamics Limb Sounder (HIRDLS) experiment on Aura, *Proc. SPIE Int. Soc. Opt. Eng.*, *5152*, 162–171.

Gille, J. C., et al. (2008), High Resolution Dynamics Limb Sounder: Experiment overview, recovery, and validation of initial temperature data, *J. Geophys. Res.*, *113*, D16S43, doi:10.1029/2007JD008824.

Gurubaran, S., T. K. Ramkumar, S. Sridharan, and R. Rajaram (2001), Signatures of quasi-2-day planetary waves in the equatorial electrojet: Results from simultaneous observations of mesospheric winds and geomagnetic field variations at low latitudes, *J. Atmos. Sol. Terr. Phys.*, *63*, 813–823.

Häusler, K., and H. Lühr (2009), Nonmigrating tidal signals in the upper thermospheric zonal wind at equatorial latitudes as observed by CHAMP, *Ann. Geophys.*, *27*, 2643–2652.

Hecht, J. H., R. L. Walterscheid, L. J. Gelinas, R. A. Vincent, I. M. Reid, and J. M. Woithe (2010), Observations of the phase-locked 2 day wave over the Australian sector using medium-frequency radar and airglow data, *J. Geophys. Res.*, *115*, D16115, doi:10.1029/2009JD013772.

Hertzog, A., G. Boccara, R. A. Vincent, F. Vial, and Ph. Coquerez (2008), Estimation of gravity-wave momentum flux and phase speeds from long-duration stratospheric balloon flights: 2. Results from the Vorcore campaign in Antarctica, *J. Atmos. Sci.*, *65*, 3056–3070.

Hoffmann, L., and M. J. Alexander (2010), Occurrence frequency of convective gravity waves during the North American thunderstorm season, *J. Geophys. Res.*, *115*, D20111, doi:10.1029/2010JD014401.

Hoffmann, P., Ch. Jacobi, and C. Borries (2012), Possible planetary wave coupling between the stratosphere and ionosphere by gravity wave modulation, *J. Atmos. Sol. Terr. Phys.*, *75-76*, 71–80, doi:10.1016/j.jastp.2011.07.008.

Holton, J. R. (1982), The role of gravity wave induced drag and diffusion in the momentum budget of the mesosphere, *J. Atmos. Sci.*, *39*, 791–799.

Holton, J. R. (1983), The influence of gravity wave breaking on the general circulation of the middle atmosphere, *J. Atmos. Sci.*, *40*, 2497–2507.

Holton, J. R. (1984), The generation of mesospheric planetary waves by zonally asymmetric gravity wave breaking, *J. Atmos. Sci.*, *41*, 3427–3430.

Huang, F. T., H. G. Mayr, C. A. Reber, J. M. Russell III, M. G. Mlynczak, and J. G. Mengel (2008), Ozone quasi-biennial oscillations (QBO), semiannual oscillations (SAO), and correlations with temperature in the mesosphere, lower thermosphere, and stratosphere, based on measurements from SABER on TIMED and MLS on UARS, *J. Geophys. Res.*, *113*, A01316, doi:10.1029/2007JA012634.

Immel, T. J., E. Sagawa, S. L. England, S. B. Henderson, M. E. Hagan, S. B. Mende, H. U. Frey, C. M. Swenson, and L. J. Paxton (2009), Control of equatorial ionospheric morphology by atmospheric tides, *Geophys. Res. Lett.*, *33*, L15108, doi:10.1029/2006GL026161.

Jacobi, Ch., K. Fröhlich, and A. Pogoreltsev (2006), Quasi two-day-wave modulation of gravity wave flux and consequences for the planetary wave propagation in a simple circulation model, *J. Atmos. Sol. Terr. Phys.*, *68*, 283–292, doi:10.1016/j.jastp.2005.01.017.

Jiang, J. H., B. Wang, K. Goya, K. Hocke, S. D. Eckermann, J. Ma, D. L. Wu, and W. G. Read (2004), Geographical distribution and interseasonal variability of tropical deep convection: UARS MLS observations and analyses, *J. Geophys. Res.*, *109*, D03111, doi:10.1029/2003JD003756.

Krebsbach, M., and P. Preusse (2007), Spectral analysis of gravity wave activity in SABER temperature data, *Geophys. Res. Lett.*, *34*, L03814, doi:10.1029/2006GL028040.

Lieberman, R. S. (1999), Eliassen-Palm fluxes of the 2-day wave, *J. Atmos. Sci.*, *56*, 2846–2861.

Lieberman, R. S. (2002), Eliassen-Palm fluxes of the 2-day wave (Corrigendum), *J. Atmos. Sci.*, *59*, 2625–2627.

Limpasuvan, V., C. B. Leovy, Y. J. Orsolini, and B. A. Boville (2000), A numerical simulation of the two-day wave near the stratopause, *J. Atmos. Sci.*, *57*, 1702–1717.

Limpasuvan, V., and D. L. Wu (2003), Two-day wave observations of UARS Microwave Limb Sounder mesospheric water vapor and temperature, *J. Geophys. Res.*, *108*(D10), 4307, doi:10.1029/2002JD002903.

Liu, G., T. J. Immel, S. L. England, K. K. Kumar, and G. Rankumar (2010), Temporal modulation of the four-peaked longitudinal structure of the equatorial ionosphere by the 2 day planetary wave, *J. Geophys. Res.*, *115*, A12338, doi:10.1029/2010JA016071.

McCormack, J. P., S. D. Eckermann, K. W. Hoppel, and R. A. Vincent (2010), Amplification of the quasi-two day wave through nonlinear interaction with the migrating diurnal tide, *Geophys. Res. Lett.*, *37*, L16810, doi:10.1029/2010GL043906.

Meyer, C. K. (1999), Gravity wave interactions with mesospheric planetary waves: A mechanism for penetration into the thermosphere-ionosphere system, *J. Geophys. Res.*, *104*, 28181–28196.

Mlynczak, M. G. (1997), Energetics of the mesosphere and lower thermosphere and the SABER instrument, *Adv. Space Res.*, *44*, 1177–1183.

Mukhtarov, P., D. Pancheva, and B. Andonov (2009), Global structure and seasonal and interannual variability of the migrating diurnal tide seen in the SABER/TIMED temperatures between 20 and 120 km, *J. Geophys. Res.*, *114*, A02309, doi:10.1029/2008JA013759.

Müller, H. (1972), Long period wind oscillations, *Phil. Trans. Roy. Soc. London*, *272*, 585-598.

Norton, W. A., and J. Thuburn (1996), The two-day wave in a middle atmosphere GCM, *Geophys. Res. Lett.*, *23*, 2113–2116.

Oberheide, J., G. A. Lehmacher, D. Offermann, K. U. Grossmann, A. H. Manson, C. E. Meek, F. J. Schmidlin, W. Singer, P. Hoffmann, and R. A. Vincent (2002), Geostrophic wind fields in the stratosphere and mesosphere from satellite data, *J. Geophys. Res.*, *107*, 8175, doi:10.1029/2001JD000655.

Oberheide, J., J. M. Forbes, K. Häusler, Q. Wu, and S. L. Bruinsma (2009), Tropospheric tides from 80 to 400 km: Propagation, interannual variability, and solar cycle effects, *J. Geophys. Res.*, *114*, D00I05, doi:10.1029/2009JD012388.

Oberheide, J., J. M. Forbes, X. Zhang, and S. L. Bruinsma (2011), Wave-driven variability in the ionosphere-thermosphere-mesosphere system from TIMED observations: What contributes to the "wave 4"?, *J. Geophys. Res.*, *116*, A01306, doi:10.1029/2010JA015911.

Offermann, D., P. Hoffmann, P. Knieling, R. Koppmann, J. Oberheide, D. M. Riggin, V. M. Tunbridge, and W. Steinbrecht (2011), Quasi 2 day waves in the summer mesosphere: Triple structure of amplitudes and long-term development, *J. Geophys. Res.*, *116*, D00P02, doi:10.1029/2010JD015051.

Orsolini, Y. S., V. Limpasuvan, and C. B. Leovy (1997), The tropical stratopause in the UKMO stratospheric analyses: Evidence for a 2-day wave and inertial circulations, *Q. J. R. Meteorol. Soc.*, *123*, 1707–1724.

Pancheva, D. V., P. J. Mukhtarov, M. G. Shepherd, N. J. Mitchell, D. C. Fritts, D. M. Riggin, S. J. Franke, P. P. Batista, M. A. Abdu, I. S. Batista, B. R. Clemesha, and T. Kikuchi (2006), Two-day wave coupling of the low-latitude atmosphere-ionosphere system, *J. Geophys. Res.*, *111*, A7313, doi:10.1029/2005JA011562.

Pancheva, D. V., P. Mukhtarov, B. Andonov, N. J. Mitchell, and J. M. Forbes (2009a), Planetary waves observed by TIMED/SABER in coupling the stratosphere-mesosphere-lower thermosphere during the winter of 2003/2004: Part 1. Comparison with the UKMO temperature results, *J. Atmos. Sol. Terr. Phys.*, *71*, 61–74, doi:10.1016/j.jastp.2008.09.016.

Pancheva, D. V., P. Mukhtarov, B. Andonov, N. J. Mitchell, and J. M. Forbes (2009b), Planetary waves observed by TIMED/SABER in coupling the stratosphere-mesosphere-lower thermosphere during the winter of 2003/2004: Part 2. Altitude and latitude planetary wave structure, *J. Atmos. Sol. Terr. Phys.*, *71*, 75–87, doi:10.1016/j.jastp.2008.09.027.

Pancheva, D., P. Mukhtarov, and B. Andonov (2010), Global structure, seasonal and interannual variability of the eastward propagating tides seen in the SABER/TIMED temperatures (2002–2007), *Adv. Space Res.*, *46*, 257–274, doi:10.1016/j.asr.2010.03.026.

Pedatella, N. M., and J. M. Forbes (2012), The quasi 2 day wave and spatial-temporal variability of the OH emission and ionosphere, *J. Geophys. Res.*, *117*, A01320, doi:10.1029/2011JA017186.

Pendlebury, D. (2012), A simulation of the quasi-two-day wave and its effect on variability of summertime mesopause temperatures, *J. Atmos. Sol. Terr. Phys.*, *80*, 138–151, doi:10.1016/j.jastp.2012.01.006.

Pfister, L. (1985), Baroclinic instability of easterly jets with applications to the summer mesosphere, *J. Atmos. Sci.*, *42*, 313–330.

Plumb, R. A. (1983), Baroclinic instability of the summer mesosphere: A mechanism for the quasi-two-day wave?, *J. Atmos. Sci.*, *40*, 262–270.

Preusse, P., S. D. Eckermann, J. Oberheide, M. E. Hagan, and D. Offermann (2001), Modulation of gravity waves by tides as seen in CRISTA temperatures, *Adv. Space Res.*, *27*, 1773–1778.

Preusse, P., A. Dörnbrack, S. D. Eckermann, M. Riese, B. Schaeler, J. T. Bacmeister, D. Broutman, and K. U. Grossmann (2002), Space-based measurements of stratospheric mountain waves by CRISTA, 1. Sensitivity, analysis method, and a case study, *J. Geophys. Res.*, *107*(D23), 8178, doi:10.1029/2001JD000699.

Preusse, P., et al. (2006), Tropopause to mesopause gravity waves in August: Measurement and modeling, *J. Atmos. Sol. Terr. Phys.*, *68*, 1730–1751, doi:10.1016/j.jastp.2005.10.019.

Preusse, P., S. D. Eckermann, and M. Ern (2008), Transparency of the atmosphere to short horizontal wavelength gravity waves, *J. Geophys. Res.*, *113*, D24104, doi:10.1029/2007JD009682.

Preusse, P., S. Schroeder, L. Hoffmann, M. Ern, F. Friedl-Vallon, H. Oelhaf, H. Fischer, and M. Riese (2009a), New perspectives on gravity wave remote sensing by spaceborne infrared limb imaging, *Atmos. Meas. Tech.*, *2*, 299–311.

Preusse, P., S. D. Eckermann, M. Ern, J. Oberheide, R. H. Picard, R. G. Roble, M. Riese, J. M. Russell III, and M. G. Mlynczak (2009b), Global ray tracing simulations of the SABER gravity wave climatology, *J. Geophys. Res.*, *114*, D08126, doi:10.1029/2008JD011214.

Randel, W. J. (1994), Observations of the 2-day wave in NMC stratospheric analyses, *J. Atmos. Sci.*, *51*, 306–313.

Randel, W., M.-L. Chanin, and C. Michaut (2002), SPARC intercomparison of middle atmosphere climatologies, WCRP–116, WMO/TD–No. 1142, SPARC report No. 3.

Randel, W., et al. (2004), The SPARC intercomparison of middle atmosphere climatologies, *J. Clim.*, *17*, 986–1003.

Remsberg, E. E., L. L. Gordley, B. T. Marshall, R. E. Thompson, J. Burton, P. Bhatt, V. L. Harvey, G. Lingenfelser, and M. Natarajan (2004), The Nimbus 7 LIMS version 6 radiance conditioning and temperature retrieval methods and results, *J. Quant. Spectrosc. Radiat. Transfer*, *86*, 395–424, doi:10.1016/j.jqsrt.2003.12.007.

Remsberg, E. E., et al. (2008), Assessment of the quality of the Version 1.07 temperature-versus-pressure profiles of the middle atmosphere from TIMED/SABER, *J. Geophys. Res.*, *113*, D17101, doi:10.1029/2008JD010013.

Rojas, M., and W. Norton (2007), Amplification of the 2-day wave from mutual interaction of global Rossby-gravity and local modes in the summer mesosphere, *J. Geophys. Res.*, *112*, D12114, doi:10.1029/2006JD008084.

Russell III, J. M., M. G. Mlynczak, L. L. Gordley, J. Tansock, and R. Esplin (1999), An overview of the SABER experiment and preliminary calibration results, *Proc. SPIE Int. Soc. Opt. Eng.*, *3756*, 277–288.

Salby, M. L. (1984), Survey of planetary-scale traveling waves: The state of theory and observations, *Rev. Geophys.*, *22*, 209–236.

Salby, M. L., and P. F. Callaghan (2001), Seasonal amplification of the 2-day wave: Relationship between normal mode and instability, *J. Atmos. Sci.*, *58*, 1858–1869.

Salby, M. L., and P. F. Callaghan (2008), Interaction of the 2-day wave with solar tides, *J. Geophys. Res.*, *113*, D14121, doi:10.1029/2006JD007892.

Sato, K., S. Watanabe, Y. Kawatani, Y. Tomikawa, K. Miyazaki, and M. Takahashi (2009), On the origins of mesospheric gravity waves, *Geophys. Res. Lett.*, *36*, L19801, doi:10.1029/2009GL039908.

Schwartz, M. J., et al. (2008), Validation of the Aura Microwave Limb Sounder temperature and geopotential height measurements, *J. Geophys. Res.*, *113*, D15S11, doi:10.1029/2007JD008783.

Swinbank, R., and D. A. Ortland (2003), Compilation of wind data for the Upper Atmosphere Research Satellite (UARS) Reference Atmosphere Project, *J. Geophys. Res.*, *108*, 4615, doi:10.1029/2002JD003135.

Thayaparan, T., W. K. Hocking, J. MacDougall, A. H. Manson, and C. E. Meek (1997), Simultaneous observations of the 2-day wave at London (43 ° N, 81 ° W), and Saskatoon (52 ° N, 107 ° W) near 91 km altitude during the two years of 1993 and 1994, *Ann. Geophys.*, *15*, 1324–1339.

Tunbridge, V. M., D. J. Sandford, and N. J. Mitchell (2011), Zonal wavenumbers of the summertime 2 day planetary wave observed in the mesosphere by EOS Aura Microwave Limb Sounder, *J. Geophys. Res.*, *116*, D11103, doi:10.1029/2010JD014567.

Warner, C. D., A. A. Scaife, and N. Butchart (2005), Filtering of parameterized nonorographic gravity waves in the Met Office unified model, *J. Atmos. Sci.*, *62*, 1831–1848.

Wright, C. J., and J. C. Gille (2011), HIRDLS observations of gravity wave momentum fluxes over the monsoon regions, *J. Geophys. Res.*, *116*, D12103, doi:10.1029/2011JD015725.

Wu, D. L., E. F. Fishbein, W. G. Read, and J. W. Waters (1996), Excitation and evolution of the quasi-2-day wave observed in UARS/MLS temperature measurements, *J. Atmos. Sci.*, *53*, 728–738.